Final Technical Report

Project Title: Impacts of stratification and non-equilibrium winds and waves on hub-height winds

DOE Award Number: DE-EE0005373

Project Period: September 30, 2011 - March 31, 2015

Principal Investigator: Edward G. Patton
⟨patton@ucar.edu⟩
(303) 497-8958

Organization: University Corporation for Atmospheric Research
National Center for Atmospheric Research
3090 Center Green Drive
Boulder, Colorado, 80301

Co-Investigators: Branko Kosović, National Center for Atmospheric Research
Peter Sullivan, National Center for Atmospheric Research
Jimy Dudhia, National Center for Atmospheric Research
Larry Mahrt, Northwest Research Associates
Mark Žagar, Vestas Wind Systems A/S
Line Gulstad, Vestas Wind Systems A/S

Date of Report: July 14, 2015

Acknowledgment: This report is based upon work supported by the U.S. Department of Energy under Award No. DE-EE0005373.

Contents

List of Acronyms

ABL atmospheric boundary layer

ASIT Air-Sea Interaction Tower

CBLAST-Low Coupled Boundary Layers Air-Sea Transfer - Low Wind

FINO1 Forschungsplattformen in Nord- und Ostsee Nr. 1

IEC International Electrotechnical Commission

LES large-eddy simulation

LiDAR light detection and ranging

MAE mean absolute error

MOST Monin-Obukhov Similarity Theory

MYNN Mellor-Yamada-Nakanishi-Niino

NCEP National Center for Environmental Prediction

OISST Optimum Interpolation Sea Surface Temperature

RMSE root mean square error

SST sea surface temperature

TI turbulence intensity

UAV unmanned aerial vehicle

WAMOS-II Wave and Surface Current Monitoring System

WAsP Wind Atlas Analysis and Application Program

WRF Weather and Research Forecasting

WRF-SCM WRF Single Column Model

List of Figures

List of Tables

1. Executive Summary

This project used a combination of turbulence-resolving large-eddy simulations, single-column modeling (where turbulence is parameterized), and currently available observations to improve, assess, and develop a parameterization of the impact of non-equilibrium wave states and stratification on the buoy-observed winds to establish reliable wind data at the turbine hub-height level.

Analysis of turbulence-resolving simulations and observations illuminates the non-linear coupling between the atmosphere and the undulating sea surface. This analysis guides modification of existing boundary layer parameterizations to include wave influences for upward extrapolation of surface-based observations through the turbine layer. Our surface roughness modifications account for the interaction between stratification and the effects of swell's amplitude and wavelength as well as swell's relative motion with respect to the mean wind direction.

The single-column version of the open source Weather and Research Forecasting (WRF) model (Skamarock et al., 2008) serves as our platform to test our proposed planetary boundary layer parameterization modifications that account for wave effects on marine atmospheric boundary layer flows. WRF has been widely adopted for wind resource analysis and forecasting. The single-column version is particularly suitable to development, analysis, and testing of new boundary layer parameterizations. We utilize WRF's single-column version to verify and validate our proposed modifications to the Mellor-Yamada-Nakanishi-Niino (MYNN) boundary layer parameterization (Nakanishi and Niino, 2004). We explore the implications of our modifications for two-way coupling between WRF and wave models (*e.g.,*Wavewatch III). The newly implemented parameterization accounting for marine atmospheric boundary layer-wave coupling is then tested in three-dimensional WRF simulations at grid sizes near 1 km. These simulations identify the behavior of simulated winds at the wind plant scale.

Overall project conclusions include:

- In the presence of fast-moving swell (significant wave height H_s = 6.4 m, and phase speed c_p = 18 $\mathrm{m\,s^{-1}}$), the atmospheric boundary layer grows more rapidly when waves propagate opposite to the winds compared to when winds and waves are aligned. Pressure drag increases by nearly a factor of 2 relative to the turbulent stress for the extreme case where waves propagate at 180° compared to the pressure gradient forcing. Net wind speed reduces by nearly 15% at hub-height for the 180°-case compared to the 0°-case, and turbulence intensities increase by nearly a factor of 2. These impacts diminish with decreasing wave age.

- Stratification increases hub height wind speeds and increases the vertical shear of the mean wind across the rotor plane. Fortuitously, this stability-induced enhanced shear does not influence turbulence intensity at hub height, but does increase (decrease) turbulence intensity below (above) hub height. Increased stability also increases the wave-induced pressure stress by $\sim$10%.

- Off the East Coast of the United States during Coupled Boundary Layers Air-Sea Transfer - Low Wind (CBLAST-Low), cases with short fetch include thin stable boundary layers with depths of only a few tens of meters. In the coastal zone, the relationship between the mean wind and the surface fiction velocity ($u_*(V)$) is significantly related to wind direction for weak winds but is not systematically related to the air sea difference of virtual potential temperature, $\delta\theta_v$; since waves generally propagate from the south at the Air-Sea Interaction

Tower (ASIT) tower, these results suggest that under weak wind conditions waves likely influence surface stress more than stratification does.

- Winds and waves are frequently misaligned in the coastal zone. Stability conditions persist for long duration. Over a four year period, the Forschungsplattformen in Nord- und Ostsee Nr. 1 (FINO1) tower (a site with long fetch) primarily experienced weakly-unstable conditions, while stability at the ASIT tower (with a larger influence of offshore winds) experiences a mix of both unstable and stable conditions, where the summer months are predominantly stable.

Wind-wave misalignment likely explains the large scatter in observed non-dimensional surface roughness under swell-dominated conditions. Andreas et al.'s (2012) relationship between u_* and the 10-m wind speed under predicts the increased u_* produced by wave-induced pressure drag produced by misaligned winds and waves. Incorporating wave-state (speed and direction) influences in parameterizations improves predictive skill. In a broad sense, these results suggest that one needs information on winds, temperature, and *wave state* to upscale buoy measurements to hub-height and across the rotor plane. Our parameterization of wave-state influences on surface drag has been submitted for inclusion in the next publicly available release.

In combination, our project elucidates the impacts of two important physical processes (non-equilibrium wind/waves and stratification) on the atmosphere within which offshore turbines operate. This knowledge should help guide and inform manufacturers making critical decisions surrounding design criteria of future turbines to be deployed in the coastal zone.

Reductions in annually averaged hub height wind speed error using our new wave-state-aware surface layer parameterization are relatively modest. However since wind turbine power production depends on the wind speed cubed, the error in estimated power production is close to 5%; which is significant and can substantially impact wind resource assessment and decision making with regards to the viability of particular location for a wind plant location. For a single 30-hour forecast, significant reductions in wind speed prediction errors can yield substantially improved wind power forecast skill, thereby mitigating costs and/or increasing revenue through improved: 1) forecasting for maintenance operations and planning, 2) day-ahead forecasting for power trading and resource allocation, and 3) short-term forecasting for dispatch and grid balancing.

2. Introduction

2.1 Project Overview and Relevance

Accurate characterization and modeling of the wind and sea state will directly reduce the current market barriers of offshore wind and impact the overall acceleration of offshore wind deployment in the United States. The uncertainty in wind and wake model predictions is a major uncertainty in the prediction of wind power output, and therefore a deterrent to offshore wind prospecting in the United States.

For a wind power plant developer, accurate characterization of the coupling between wind and wave states is crucial for: 1) reducing uncertainty in determining an offshore wind plant location, 2) determining wind power plant layout and interaction between the turbines, 3) scheduling routine turbine maintenance, and 4) improving accuracy in the calculation of load estimates and energy production for a proposed offshore wind project. Advancing research and reducing uncertainty in these areas will provide wind power plant developers and project financiers with more confidence, reliability and predictability for choosing offshore wind power plant production over other energy production sources.

The demand for accurate numerical estimates of wind speed, wind shear and turbulence intensity at hub-height and across the rotor plane are more vital for offshore wind vs. on-shore wind due to: 1) the complex coupling between wave and wind states, and 2) the heightened need for accurate energy production estimates on the more expensive and typically larger MW offshore wind turbine parks. A 1 $\mathrm{m\,s^{-1}}$ forecasting error in mean wind speed, for example, can result in significant losses in expected energy production revenue and/or erroneously lead a wind developer into choosing a wind turbine generator based upon a misidentified International Electrotechnical Commission (IEC) wind class for the site.

For this reason, our research project focused on improved modeling of the atmospheric response to stratification and non-equilibrium wind and sea-states in an effort to expedite the deployment of offshore wind.

2.2 Market Barriers

Removing market barriers hindering wider deployment of offshore wind power generation capacity requires bridging several gaps in our understanding of the fundamental processes coupling the ocean and the atmosphere affecting the hub height wind resource. Reducing the cost of deployment and operation of offshore wind farms can be achieved through improved: 1) energy resource planning, 2) wind resource characterization, and 3) overall system performance through better siting and energy capture. One path to achieve these goals involves improved algorithms to estimate hub-height wind speed from surface measurements to more accurately assess and predict the wind resource.

Accurate hub-height wind data are essential in assessing the cost, energy production and design requirements for offshore wind farms. We therefore propose to carry out research toward better understanding of the offshore atmospheric boundary layer that will enable us to develop a state-of-the-science algorithm for accurate determination of site-specific wind characteristics based on limited surface measurements. The proposed development reduces the need for extensive and expensive meteorological measurements as envisioned by Musial and Ram (2010).

Through our research, we advance the understanding of the offshore operating environment and develop an algorithm for accurate wind speed estimation across the turbine layer. The new algorithm and corresponding parameterization has been implemented in the WRF mesoscale model (Skamarock et al., 2008). In this way, the proposed effort enables more accurate and reliable mesoscale prediction and thus provide information to support economic decisions, turbine siting, and offshore wind power technology development.

3. Background

3.1 Non-equilibrium Boundary Layers Over Coastal Waters

It is well known that fluctuations in the turbulent atmosphere interacting with a water surface beneath it can initiate surface gravity wave growth (*e.g.,* Phillips, 1977), where the scale, phase, and speed of the waves grown depend strongly on the strength and directionality of the mean wind. High winds in one location can generate large, rapidly traveling waves that can persist over extended periods and travel great distances such that at any given location, the current wave-state is rarely in strict wind-wave equilibrium. Wind-wave equilibrium is realized when winds blow with sufficient stationarity that the wave spectrum does not change with fetch (or distance from shore), i.e. the wind input is balanced by wave dissipation and non-linear interactions in the wave action equation (*e.g.,* Csanady, 2001).

Recent observations (Smedman et al., 2009), turbulence closure modeling (Hanley and Belcher, 2008), and turbulence-resolving simulations (*e.g.,* Sullivan et al., 2008, 2010) all show that these fast moving water waves generated far from shore (*i.e.* swell) significantly impact boundary layer winds by imparting an upward flux of momentum from the ocean to the atmosphere. No matter the wind speed, as long as the waves are moving faster than the wind, non-equilibrium waves dramatically modify the relationship between surface and hub-height winds, and therefore hub-height turbulence levels. The marine atmospheric boundary layer typically exhibits much shallower depths than those occurring over land, particularly during daytime periods; hence the character of the underlying surface is felt though a much greater percentage of the marine atmospheric boundary layer than of the atmospheric boundary layer over land. In general, turbulence over water is weaker than that over land, which can also contribute to the persistence of turbine wakes.

Much of what is currently known regarding the coupling between the marine atmospheric boundary layer and the underlying surface gravity wave field relies on the assumption of wind-wave equilibrium. However, wind-wave equilibrium is generally not achieved in coastal zones where future U.S. offshore turbine deployments are likely to be located (Hanley et al., 2010). Coastal regions especially depart from wind-wave equilibrium due to: 1) diurnal forcing associated with the daily sea breeze, 2) a shallow water column which limits wave growth, and 3) distant storms generating high-amplitude swell that arrives in coastal regions often dominating the local wave state. Two critical aspects of wind-wave coupling remain largely understudied:

Stratification: Over land, it is well known that thermal stratification modifies the atmosphere, its momentum transport capabilities and characteristics, and therefore how it couples with the surface. Sea surface temperatures typically reflect variations on seasonal timescales, but through the interaction between ocean currents, surface waves, and the shoreline, the ocean surface can exhibit strong sea surface temperature gradients occurring over much shorter time-scales (hours to days) and with sufficiently large amplitude to modify the overlying atmosphere (*e.g.,* Skyllingstad et al., 2007). How the turbulent wind overlying a swell-dominated water surface responds to thermal forcing has not been clearly established. Does stratification influence the height to which the non-equilibrium wave forcing is felt?

Swell orientation to the mean wind: Most analysis of winds and turbulence over swell-dominated surfaces thus far has ignored the non-local origin of swell and the frequent nonalignment of the swell with the wind. How the wind responds to misalignment of the surface waves and how to incorporate the wind's response in parameterizations used to relate surface-observations to hub-height is unclear.

Marine atmospheric boundary layer parameterizations are currently used 1) to correlate the buoy measurements with the wind and turbulence profiles aloft, and 2) to represent the dynamical coupling between the overlying flow and the water surface in numerical weather prediction models. The current parameterizations do not account for the coupled influences of stratification and non-equilibrium wave states on the marine boundary layer structure. Recent studies (*e.g.,* Tambke et al., 2005) show that parameterizations used to represent marine boundary layer winds/turbulence commonly result in a significant root mean square error ($\sim 3\ \mathrm{m\,s^{-1}}$ for a 48-hour forecast). Substantial deviations from expected wind profile shapes were observed across a wide range of atmospheric stability conditions. Such errors indicate that current approaches to modeling the marine atmospheric boundary layer (*i.e.* those based on simple power law wind profile assumptions such as Wind Atlas Analysis and Application Program (WAsP), or on Monin-Obukhov Similarity Theory (MOST)) do not accurately account for wind-wave coupling (Smedman et al., 2009). Since the power at a wind turbine is a function of the wind speed cubed, such significant uncertainty in hub-height wind forecasts is not acceptable for operational use.

3.2 Approach

This project used a combination of turbulence-resolving large-eddy simulations, single-column modeling (where turbulence is parameterized), and currently available observations to improve, assess, and develop a parameterization of the impact of non-equilibrium wave states and stratification on the buoy-observed winds to establish reliable wind data at the turbine hub-height level.

Analysis of turbulence-resolving simulations and observations illuminates the non-linear coupling between the atmosphere and the undulating sea surface. This analysis guides modification of existing boundary layer parameterizations to include wave influences for upward extrapolation of surface-based observations through the turbine layer. Our surface roughness modifications account for the interaction between stratification and the effects of swell's amplitude and wavelength as well as swell's relative motion with respect to the mean wind direction.

The single-column version of the open source WRF model (Skamarock et al., 2008) serves as our platform to test our proposed planetary boundary layer parameterization modifications that account for wave effects on marine atmospheric boundary layer flows. WRF has been widely adopted for wind resource analysis and forecasting. The single-column version is particularly suitable to development, analysis, and testing of new boundary layer parameterizations. We utilize WRF's single-column version to verify and validate the proposed modifications to the MYNN boundary layer parameterization (Nakanishi and Niino, 2004). We explore the implications of our modifications for two-way coupling between WRF and wave models (*e.g.,*Wavewatch III). The newly implemented parameterization accounting for marine atmospheric boundary layer-wave coupling is then tested in three-dimensional WRF simulations at grid sizes near 1 km. These simulations identify the behavior of simulated winds at the wind plant scale.

4. Results and Discussion

4.1 ASIT / CBLAST-Low Observations (East Coast of the United States)

4.1.1 Data description

LongEZ data: We analyze data collected by the LongEZ aircraft operated by Tim Crawford for the pilot program of CBLAST-Low conducted over the Atlantic Ocean south of Martha's Vineyard Island, MA, USA, during July–August 2001. The data were collected at a rate of 50 samples per second with a flight air speed of about 50 $\mathrm{m\,s^{-1}}$, which corresponds to a horizontal interval of about 1 m between data measurements. Winds were measured using the BAT probe (Crawford and Dobosy, 1992), positioned 2 m in front of the nose and five wing widths ahead of the canard. Fast-response temperature was measured using a 0.13-mm micro-bead thermistor mounted inside the design stagnation point port on the BAT hemisphere. Height above the sea surface was measured by a NovAtel GPS sensor and calibrated with a Riegl laser (LD90-3100 VHS). The LongEZ instrumentation is described further in Sun et al. (2001) and Mahrt et al. (2014). We analyze the 13 flights with sufficient measurements below 12 m. Based on the dependence of the fluxes on the averaging width, we choose 100 mm as the width of the averaging windows. This is the smallest averaging length that included almost all of the momentum flux. Use of larger averaging lengths and potential inclusion of non-turbulent motions as part of the perturbation flow can cause local random flux that is converted to systematic error in the computation of u_* (Mahrt, 2010). For our study of stable conditions, we require that the air sea temperature difference, $\delta\theta_v$, > 0.1 K and require that the flight level is below 12 m.

ASIT data: Data from the ASIT tower collected during the CBLAST-Low experiment in late summer of 2003 (Edson et al., 2007) are also analyzed. The tower is located 3 km south of Martha's Vineyard in 15 m of water. The 20-Hz turbulence measurements were collected using CSAT3 sonic anemometers (Campbell Scientific, Inc.). Here, we analyze data from the CSAT3 anemometer measurements approximately 6 m above the mean sea surface to calculate eddy-correlation fluxes of momentum, heat virtual heat. The exact height above the sea varies with the tidal cycle and occasionally with storm tides. Slow response measurements of temperature and humidity (Vaisala RH/T sensors) at 7 m are used to compute the mean temperature for the air sea temperature difference and specific humidity. The sea surface temperature (SST) was measured by a Heitronics KT15 radiometer using an Eppley PIR to correct for sky reflections. In addition to the nominal quality control that eliminated meteorologically impossible values, data with wind direction between 0° and 150° were eliminated to reduce the effects of flow distortion by the tower.

For physical understanding, estimating the stratification within the atmosphere based on the temperature difference between two atmospheric levels on the tower would be preferable to using the air sea temperature difference because it would include short term variations of the stratification that are not necessarily captured using the SST particularly for stable conditions where the communication between the air and SST can slow. However, because the lowest temperature level is 7 m, only the atmospheric stratification above 7 m can be estimated. In addition, the temperature differences between two levels on the tower are relatively small and vulnerable to instrument errors. Our study therefore estimates the stratification as the difference between the 9 m virtual potential temperature and the surface virtual potential temperature, symbolized here as $\delta\theta_v$. The surface

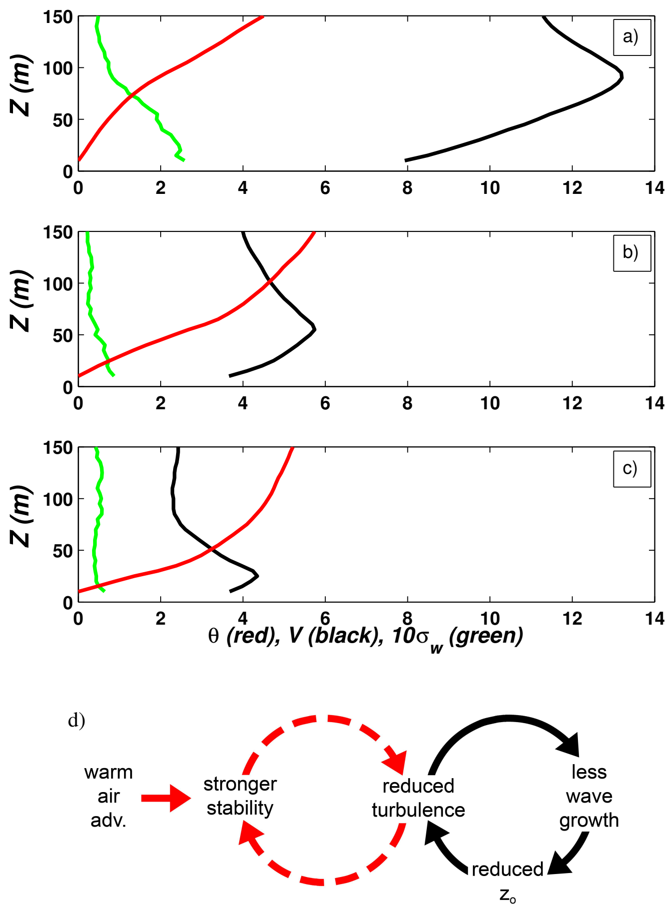

Figure 1: Grid-interpolated values composited over numerous slant aircraft soundings collected during CBLAST-Low under: a) weakly stable conditions on 7 August 2001, b) moderately stable conditions on 8 August 2001, and c) very stable conditions on 8 August 2001. Each panel shows composited wind speed, V (black, $\mathrm{m\,s^{-1}}$); potential temperature, θ (red, K); and $10 \times \sigma_w$ (green, $\mathrm{m\,s^{-1}}$). Potential temperature is the deviation from the value at the lowest level. d) A sketch of feedback mechanisms with flow of warm air over colder water. The thermal cycle is indicated by the red dashed loop where warm air advection and associated stratification suppresses the turbulence. The reduced vertical mixing allows more effective stabilizing of the flow. The mechanical cycle is designated by the solid black loop. The reduced turbulence leads to less wave development and smaller surface roughness, which in turn lead to less turbulent mixing. The separation of thermal and mechanical loops is to simplify the conceptual picture. Both loops are fully coupled at all stages.

virtual potential temperature is simply computed in terms of the saturation specific humidity for the sea surface temperature. We implicitly assume that stratification of the air near the surface is related to $\delta\theta_v$. The impact of water vapor is included because the turbulence kinetic energy is converted to potential energy through the buoyancy flux. Our use of the term *stratification* will refer to $\delta\theta_v$. Although $\delta\theta_v$ can be significantly different from $\delta\theta$ for individual data points. We neglect the small difference between the sonic virtual heat flux and the actual virtual heat flux.

We have also analyzed wave data from a subsurface node 1.5 km offshore in the Atlantic recorded by Martha's Vineyard Coastal Observatory (MVCO, http://www.whoi.edu/mvco). During the field program, the swell propagation direction was almost always out of the south with phase speeds between 6 and 8 $\mathrm{m\,s^{-1}}$. We use this information in interpretation of our analyses from the tower. However, we are uncertain if the small variations of swell propagation speed and direction are within the accuracy of the data and do not include analysis of these small variations. There are not enough data with swell propagation from other directions to satisfy even lenient sampling criteria. Regrettably, the wave measurements are not co-located with the ASIT tower and do not allow attempts to isolate the wave coherent velocity fluctuations.

4.1.2 Data analysis

Our analysis of CBLAST-Low data reveals frequent cases of warm air advection over colder water leading to stable stratification in the marine boundary layer and partial collapse of the surface wind and wave field, decoupling, and forming low-levels jets in the range of heights coinciding with the modern wind turbine rotor plane. Such common low-level jets complicate assessment of wind climatology at hub height as well as operationally forecasting winds at hub heights.

Vertical structure: The marine boundary layer's vertical structure varies with stability (Fig. 1). The weakly stable regime (Fig. 1a) is associated with surface flow from the south-southwest, which advects air from warmer water. Under these conditions, a well-defined wind maximum occurs at about 100 m and caps a partially mixed boundary layer where the stratification is modest. Some of the individual soundings included in this composite average have the low-level wind maxima are less sharp than that shown in Fig. 1a. The flow above the wind maximum is more significantly stratified, suggesting a diffuse capping inversion. The turbulence (σ_w) in the boundary layer below the wind maximum decreases systematically with height and is much smaller above the wind maximum, consistent with the usual concept of a well-defined boundary layer.

The surface wind for the moderately stable regime (Fig. 1b) is from the west-southwest near the surface, rotates to westerly at 20 m, and is northwesterly at 150 m. This flow advects warmer air from land over cooler water although the surface trajectory from land is longer than that at the jet height. Wind directional shear is a common complication in the coastal zone. Compared to the weakly stable regime, the jet is sharper; the stratification near the surface is substantially stronger; and the height of the low-level wind maximum is lower, about 50 m compared to nearly 100 m for the weakly stable regime.

The composited flow (Fig. 1b) in the moderately stable regime is characterized by strong stratification at the surface; in contrast to the weakly stable case, the stratification decreases with height. The strong stratification near the surface presumably results partly from the sharp decrease of surface temperature and surface roughness at the coastline and the subsequent feedback loops described in Fig. 1d. The turbulence in the moderately stable boundary layer below the wind maximum is much weaker than for the weakly stable regime but decreases with height as in a traditional boundary layer.

Compared to the moderately stable regime, the inversion layer in the strongly stable regime is thinner; and the wind maximum is lower (Fig. 1c), averaging about 20 m above the sea surface. The stratification is even stronger again. The very weak turbulence does not decrease systematically with height as in a traditional turbulent boundary layer.

The low-level wind maxima are often very sharp for the moderately stable and very stable regimes (Figs. 1b–c). Sharp marine jets have been reported previously. King et al. (2008) found a remarkably sharp low-level wind maximum in warm air advection over a cooler ice shelf. Beardsley et al. (1987) and Winant et al. (1988) argued that the net influence of baroclinity and stress divergence is probably responsible for the well-defined sharp jets in their observations in the coastal zone.

The low-level jet results in strong shear below and above the wind maximum. One might expect these very sharp jets to be dynamically unstable. However, within the moderately stable and very stable regimes, the sharpness of the jet is poorly correlated to the strength of the turbulence. Short-term variations of jet sharpness appear to be out of phase with the turbulence. Sharper

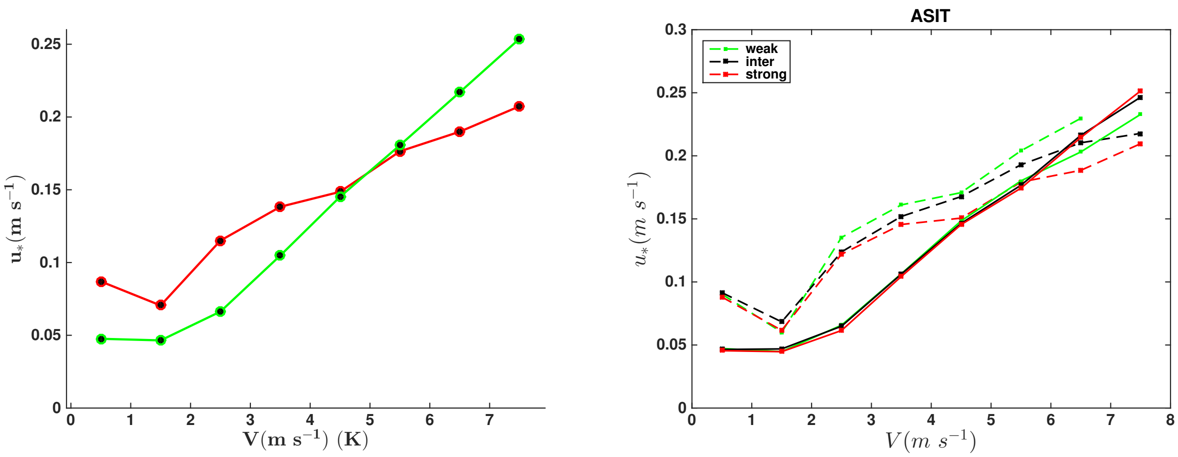

Figure 2: Left) The dependence of the interval-averaged friction velocity u_* on the mean wind speed V for northerly wind directions between 330° and 360° (red line) and southerly wind directions between 150° and 225° (green). Right) The dependence of the interval-averaged u_* on V for three classes of air sea temperature difference $\delta\theta_v$. Weak (0 K $< \delta\theta_v <$ 0.75 K, green), intermediate (0.75 K $< \delta\theta_v <$ 2.0 K, black) and strong ($\delta\theta_v >$ 2.0 K, red) stratification for wind directions between 150° and 225° (solid lines) and wind directions between 330° and 360° (dashed lines).

jets apparently produce shear-driven turbulence and diffusive smoothing of the jet followed by turbulence decay, re-sharpening of the jet, and so forth. Most low-level wind maxima are characterized by inflection points above the wind maxima. Inflection point instability may contribute to the observed turbulence above the wind maxima although definite conclusions would require three-dimensional information.

As shown in Fig. 1, these offshore low-level jets can occur at a range of heights (*i.e.* as low as 20m to as high as 150m) spanning the turbine rotor plane, which can potentially lead to substantial stress on wind turbines. Further detail on this effort can be found in Mahrt et al. (2014).

The $u_*(V)$ relationship: We now explore the relationship between $u_*(V)$ and the air-sea temperature difference. All analyses for the remainder of this study are based on the ASIT tower data where the sample size is much larger than that for the aircraft data. For $V < 4\ \mathrm{m\,s^{-1}}$, $u_*(V)$ at the 6-m level on the tower is on average significantly greater for flow with a northerly flow component compared to a southerly component (compare the red line with the green line in Fig. 2a). Possible explanations include augmentation of u_* by the propagation of swell mainly from the south against the northerly flow and reduction of u_* in wind following swell from the south. For $V > 6\ \mathrm{m\,s^{-1}}$, flow with a southerly component is characterized by larger u_* than that for flow with a northerly component, possibly related to the low amplitude of the short fetch wind-driven waves and greater averaged stratification for flow with a northerly component.

To examine the dependence of $u_*(V)$ on $\delta\theta_v$ using the tower data, the two wind direction groups are partitioned into three ranges of $\delta\theta_v$ (Fig. 2b). The influence of $\delta\theta_v$ (Fig. 2b) on u_* is detectable only for northerly flow with stronger winds where u_* for the subclass of smallest $\delta\theta_v$ (green dashed, Fig. 2b) is 10 - 15% larger than u_* for the subclass of largest $\delta\theta_v$. Contrary to similarity theory, the impact of stratification is unimportant for weaker winds.

Although the overall impact of $\delta\theta_v$ on $u_*(V)$ is undetectable for weaker winds in the present

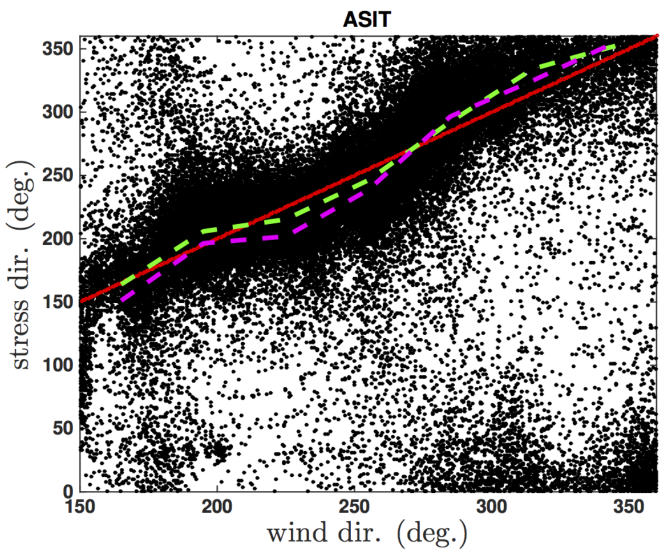

Figure 3: Relationship between the 1-min stress direction and the 1-min wind direction. The red line is the one-to-one line. The green dashed line is the stress direction computed from the stress components that were first averaged over the wind direction intervals for $V < 4$ m s^{-1}. The magenta dashed line is for $V > 4$ m s^{-1}.

data set, z/L is greater than 0.5 for about 15% of the observations with stable stratification where L is the Obukhov length. z/L becomes relatively large partly due to small u_* associated with small surface roughness over the sea The variation of z/L between 0 and 0.8 accounts for a factor of four increase of the non-dimensional shear, ϕ_m, for this data set (Edson et al., 2013). Why does this calculation indicate an important impact of stability and yet the influence of $\delta\theta_v$ on $u_*(V)$ is not evident? z/L is not a true external stability parameter and relates turbulent quantities to other turbulent quantities. Evidently, ϕ_m can depend significantly on z/L even though the direct dependence of u_* on the air-sea temperature difference is weak.

The larger $u_*(V)$ for northerly flow compared to southerly flow (Fig. 2) is consistent with the impact of the swell that normally propagates mainly from the south at this site, usually with a phase speed of about 8 m s^{-1}. The observed difference of averaged u_* between the northerly and southerly flow decreases with increasing V and reverses sign, which might be due to the expected decreased impact of swell for stronger winds and the expected increased contribution of the wind-driven waves to u_*. The increase of u_* for the interval of weakest winds with a northerly component (Fig. 2) is consistent with the influence of wave state because the effect of swell on u_* should be greatest for the weakest winds. Advection of turbulence from land could not be numerically evaluated but cannot be ruled out as a significant influence on $u_*(V)$ for northerly flow.

The stress direction is related to the wind direction for most of the measurements (Fig. 3) although the scatter is significant, where the scatter is at least partly due to the short 1-min averages, particularly for the non-stationary weaker winds. Here, the stress direction refers to the opposite direction of the stress vector. For the north-westerly flow, the stress direction tends to be directed more from the north than is the wind direction. This variation is consistent with the impact of swell from the south that would act to enhance the north-south component of the stress for a northerly flow component. For south-westerly flow, the stress direction is directed more to the south than is the wind direction, which is again consistent with the impact of northerly propagating swell on the stress direction.

This deviation of the stress direction from the wind direction does not depend significantly on the wind speed (compare magenta dashed line with green dashed line, Fig. 3). It is not known if the swell for large V can modify the stress direction more than the stress magnitude. Deviation of the

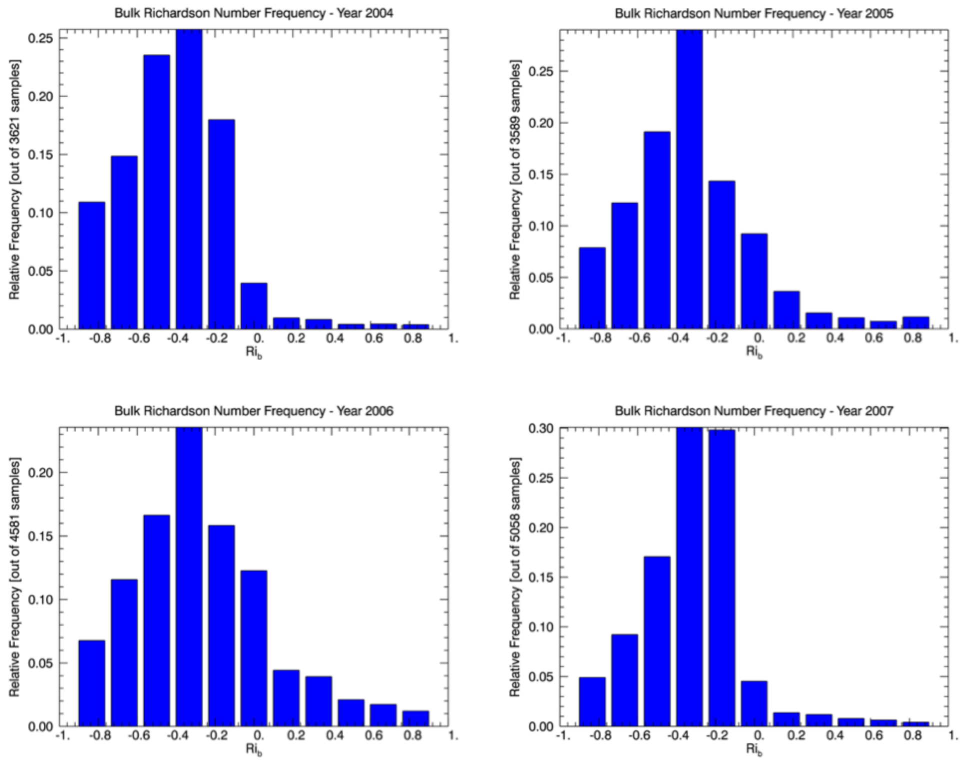

Figure 4: The relative frequency of bulk Richardson number computed from measurements of potential temperature and wind speed at 40 and 70m from FINO1 for years 2004-2007.

stress direction from the wind direction could also result from modification of the shear direction by baroclinity (Geernaert et al., 1993), Ekman effects and height-dependent advection. The data do not allow evaluation of these processes. However, the analysis in this section generally supports the expected influence of swell on the stress for weak winds.

4.2 FINO1 Observations (North Sea)

4.2.1 Data description

At FINO1 (located 45 km North of Borkum Island, N 54°0′53.5″ E 6°35′15.5″) the water depth is 30m. FINO1 has been collecting data since 2003. Wind speed is measured at eight levels using cup anemometers at heights ranging from 33 m to 100 m above sea level. Wind direction is measured with wind vanes at four levels from 33 m to 90 m above the sea level. The cup-anemometer booms face South-East, and three additional sonic-anemometer booms face North-West measuring three wind velocity components at 30 m, 50 m, and 70 m. Therefore unobstructed wind speed measurements can be constructed under a wide range of wind directions. More information regarding the FINO1 data and accessing the data can be found here: http://www.fino1.de/en/.

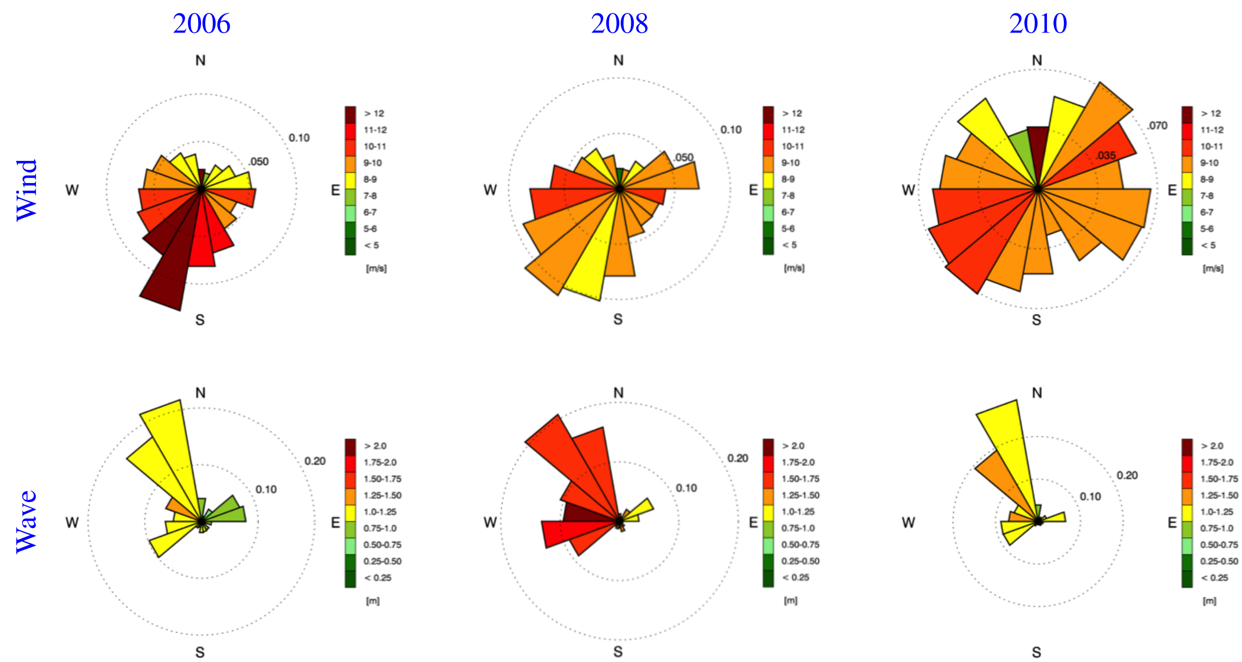

Figure 5: Wind (top row) and wave (bottom row) roses at FINO1 for 2006 (left column), 2008 (center column) and 2010 (right column).

4.2.2 Data analysis

Richardson number climatology: Barthelmie (1999) and Wharton and Lundquist (2012a,b) classify atmospheric stability ranges based on the value of the Obukhov length scale and present evidence of the effect of atmospheric stratification on the performance of wind turbines offshore and in the coastal area. However, to calculate the Obukhov length scale one needs high-rate turbulence measurements. In the absence of such high-rate measurements, atmospheric stability can be estimated by calculating bulk Richardson number, defined as

$$Ri_b = \frac{g(z_2 - z_1)}{\theta_\circ} \frac{\theta_{v_2} - \theta_{v_1}}{U_2 - U_1} \tag{1}$$

where g is the gravitational constant, $\theta_\circ$ is a reference potential temperature, and U or θ_v are the observed wind speed and virtual potential temperature, respectively, at two heights z_1 and z_2.

Atmospheric stability analysis carried out using data from the FINO platforms shows that in the North Sea shows that cold air advection over warmer ocean occurs frequently resulting in unstable atmospheric conditions (Fig. 4). This finding is consistent with Barthelmie's (1999) finding - based on one year of data - that off the coast of Denmark, stable conditions are not as common over as over land.

Winds and waves climatology: Analysis of the dominant wind directions and wind speeds at FINO1 (Fig. 5) shows that winds are generally from the South-West, but that they can come from any direction. However, surface waves generally propagate from the North-West with an average significant wave height for waves from the dominant direction of between 1.25m and 1.75m. Therefore, winds and waves at FINO1 are rarely aligned and rarely in equilibrium.

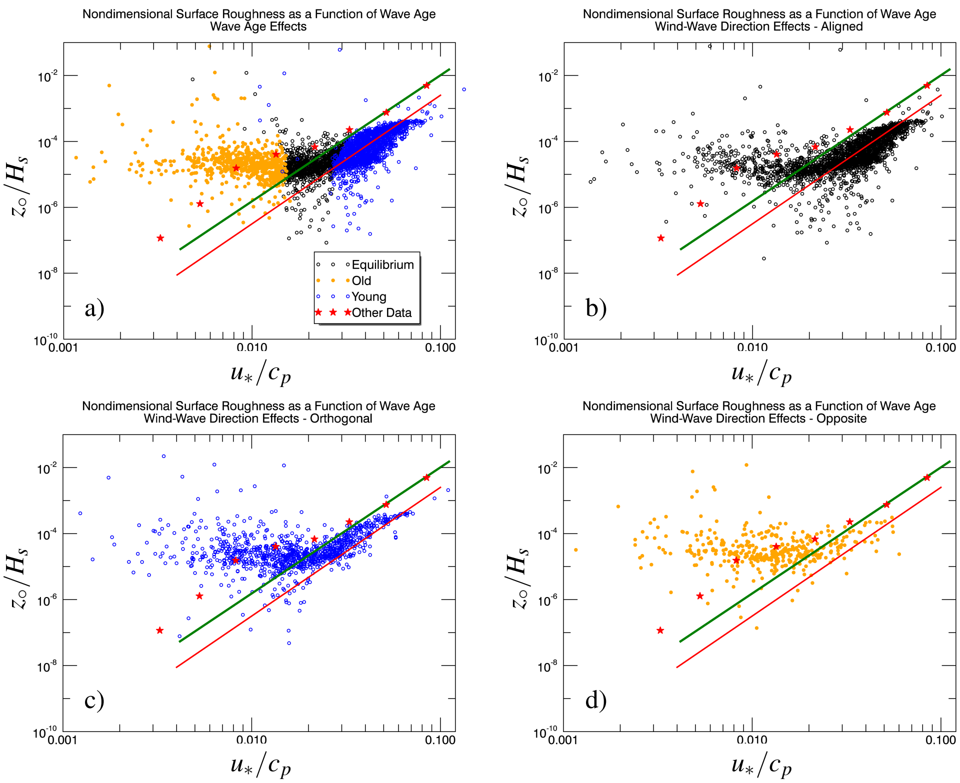

Figure 6: a) Nondimensional surface roughness length as a function of wave age from FINO1 during 2006 broken down by w_{age}. Black circles: equilibrium waves ($0.8 < w_{age} < 1.2$), orange dots: old waves ($w_{age} > 1.2$), and blue circles: young waves ($w_{age} < 0.8$) compared to data from Lange et al. (2004) (red stars) from the Rødsand field campaign in the Baltic Sea. The green line indicates the power law scaling for large u_*/c_p from the FETCH, RASEX, HEXOS, WAVES, and SWS2 field studies (Drennan et al., 2005), and the red line represents the same scaling law but using a power coefficient of 3.9 obtained from the FINO1 2006 data. b)-d) Segregating nondimensional surface roughness length according to wind/wave alignment, where winds and waves are: b) aligned, c) nearly orthogonal, and d) opposite. The colored lines and red stars in b)-d) are as described in a).

Surface roughness: Following Drennan et al. (2005), we then define a nondimensional surface roughness as the ratio of the surface roughness length to the significant wave height and plot this parameter as a function of inverse wave age (Fig. 6a). While the nondimensional surface roughness values from FINO1 tend to fall below previous observational studies (red stars), for young waves (large values of $w_{age}^{-1} = u_*/c_p$) they display similar scaling for large u_*/c_p. To more clearly demonstrate the influence of non-equilibrium winds and waves, Fig. 6a partitions the non-dimensional surface roughness by wave age; flow over old waves results in the atmosphere experiencing larger roughness than Drennan et al.'s (2005) scaling. Figures 6b-d present the nondimensional surface roughness segregated according to wind/wave alignment. The effects of alignment (or misalignment) of winds and waves are obvious: when the wave direction is opposite or nearly opposite to the wind direction, the non-dimensional roughness length reveals large scatter and no clear scaling behavior.

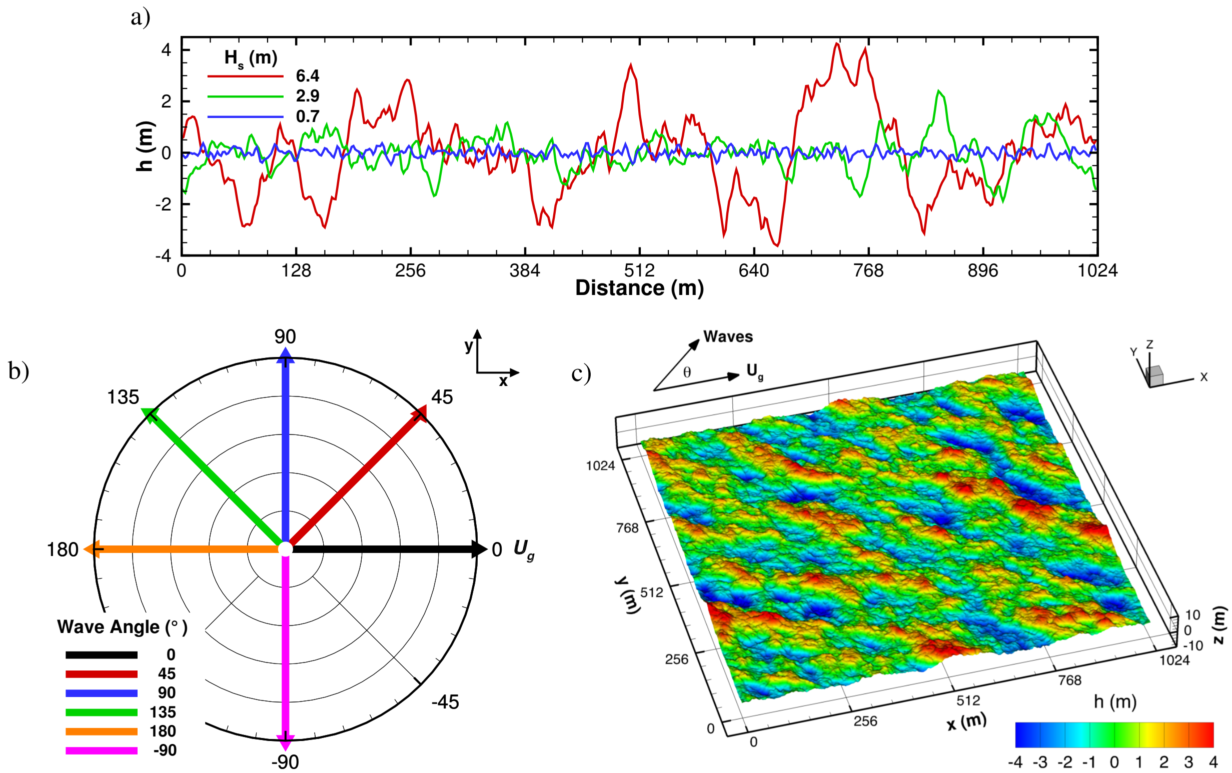

Figure 7: a) An instantaneous snapshot depicting the x-variation at a fixed y-location of the wavy surface h generated assuming wind-wave equilibrium and imposing three unique 10 m wind speeds ranging from U_{10} = (15, 10, 5) $\mathrm{m\,s^{-1}}$. Each configuration therefore produces waves with a significant wave height $H_s \sim 4\sigma_h$ = (6.4, 2.9, 0.7) m, respectively. b) Polar plot looking down from above outlining the wave propagation directions for six of the seven simulations. For reference, the pressure gradient driving the flow (U_g) is oriented in the positive x-direction (toward 0°, from left to right) in all simulations. The colored arrows show the wave's propagation direction relative to U_g. So in the 0°-case the waves are propagating in the same direction as the pressure gradient, and opposite the pressure gradient in the 180°-case. c) An example instantaneous surface (*i.e.* $h(x,y)$ at a single time t) where the waves (with H_s = 6.4 m) propagate at a 45°-angle relative to the geostrophic wind U_g, *i.e.* $\theta = 45°$.

4.3 Turbulence Resolving Simulation

4.3.1 The atmospheric LES

Explicit details outlining our computational technique can be found in Sullivan et al. (2014). Basically, we adapt our large-eddy simulation (LES) model with a flat boundary Sullivan and Patton (2011) to the situation with a three- dimensional time-dependent lower boundary with shape $h = h(x,y,t)$ by applying a transformation to the physical space coordinates $x_i \equiv (x,y,z)$ that maps them onto computational coordinates $\xi_i \equiv (\xi,\eta,\zeta)$. The computational mesh in physical space is surface following, non-orthogonal, and time varying. Vertical grid lines are held fixed at a particular (x, y) location on the surface but translate vertically as a function of time t.

4.3.2 The time varying wavy surface

The waves are generated offline following Donelan's directional spectrum (Donelan et al., 1985; Komen et al., 1994) and are assumed to be in wind-wave equilibrium (*i.e.* wave age: $c_p/U_{10} = 1.2$, where U_{10} is a specified 10 m wind speed and c_p is the phase speed of the surface waves at the spectral peak). Waves generated using three values of U_{10} are investigated: (15, 10, 5) $\mathrm{m\,s^{-1}}$. These U_{10} modifications result in waves with c_p ranging from (18, 12, 6) $\mathrm{m\,s^{-1}}$ and which produce waves with significant wave heights H_s = (6.4, 2.9, 0.7) m; using the root-mean-square elevation σ_h, $H_s = 4\sigma_h$. See Figure 7a for an example. Note that the waves in these simulations are time- and spatially-evolving, but are imposed and therefore do not respond to local wind forcing.

For each of these three wavy surfaces, six simulations are performed to investigate the impact of the wave propagation direction relative to the geostrophic wind direction; where the propagation angle varies from (0, 45, 90, 135, 180, -90) degrees (°) relative to the direction of the geostrophic wind forcing. Figures 7b,c present a schematic and example surface.

4.3.3 The simulation strategy

To generate the simulations, the NCAR large-eddy simulation code (Sullivan et al., 2014) is first configured to represent flow over a completely flat but rough surface. The domain is 1024×1024×512 $\mathrm{m^3}$, resolved by 512×512×128 grid points. The vertical coordinate uses an algebraic stretching strategy allowing fine resolution near the surface (~0.25 m) decaying with height (to ~13 m at domain top). Unresolved surface roughness is characterized using a surface roughness length $z_\circ$ = 0.0002 m. The simulations are presumed to take place at approximately 45° N latitude where the Coriolis parameter $f = 1 \times 10^{-4}\ \mathrm{s^{-1}}$. The initial virtual potential temperature profile is constant at 290 K throughout the lowest 100 m, above which the profile increases at a rate of 0.003 K $\mathrm{m^{-1}}$.

Turbulence in the flat-domain simulations is initiated by placing randomly-distributed divergence-free fluctuations on the horizontal-velocity and temperature fields and imposing a small horizontally-homogeneous surface buoyancy flux (10 W $\mathrm{m^{-2}}$) for the first 20000 time steps (approximately 1800 s). After these initial 20000 time steps, the surface buoyancy flux is set to 0 W $\mathrm{m^{-2}}$, *i.e.* the water surface temperature matches the air temperature, and the solutions are integrated forward for an additional 80000 time steps (or a total of approximately 2.5 hours) to allow the buoyancy influences to dissipate and for the turbulence to reach equilibrium with the imposed forcing. At this time, a flat-domain data set is saved.

Most of the wavy simulations are initiated from this flat-domain data set that was generated using a geostrophic wind forcing of (U_g, V_g) = (10, 0) $\mathrm{m\,s^{-1}}$. In order to expand the investigation across sufficient wave age and stability, two additional flat-domain simulations were conducted: 1) another near-neutral stability simulation, but with (U_g, V_g) = (5, 0) $\mathrm{m\,s^{-1}}$, and 2) another using the original (U_g, V_g) = (10, 0) $\mathrm{m\,s^{-1}}$ geostrophic wind forcing, but where the underlying surface is cooled at a rate of 0.25 K $\mathrm{hr^{-1}}$ (similar to Beare et al., 2006).

For each H_s and θ simulated, the waves are gradually grown into the flat-domain flow fields over a period of 400 s and each of the simulations are integrated forward for an additional 1-2×10^5 time steps. Due to the rapidly varying underlying surface, the time steps decrease such that the wavy simulations are integrated over approximately 1.5-2 hours of simulated time. Table 1 outlines the simulations conducted.

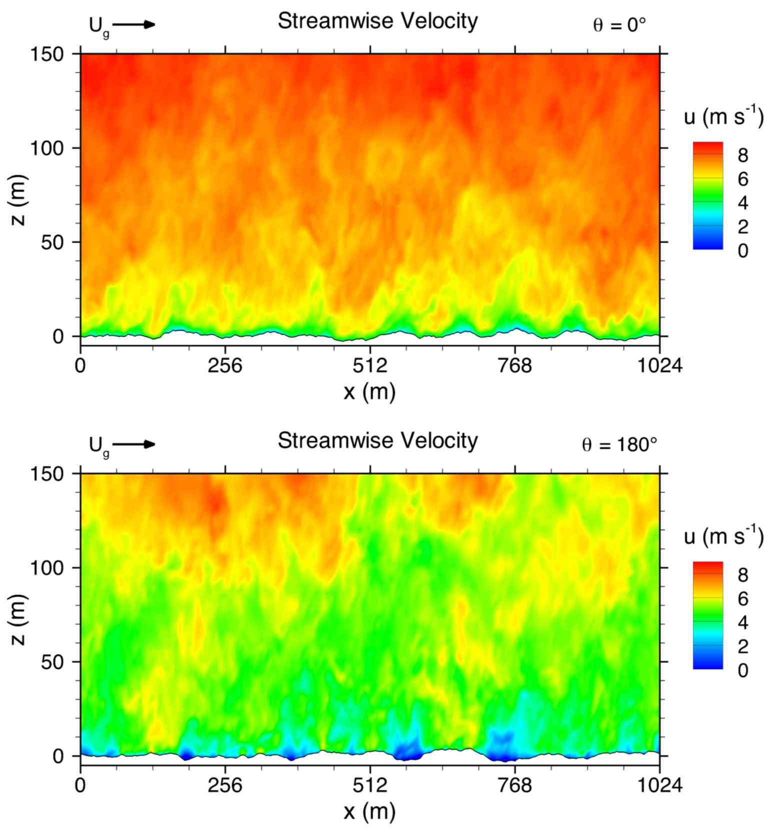

Figure 8: Instantaneous vertical slices of streamwise wind velocity from two simulations where (U_g, V_g) = (10, 0) $\mathrm{m\,s^{-1}}$ and H_s = 6.4 m for both cases. The upper panel is for $\theta = 0°$ (waves propagating with the wind), and the lower panel is for $\theta = 180°$ (waves propagating against the wind. The scales are the same between the two figures. Only the lowest 150 m of the domain is presented.

4.3.4 Influence of wind-wave alignment

In this section, we focus our attention on six simulations. These simulations are all driven by the same geostrophic winds ($[U_g, V_g]$ = [10, 0] $\mathrm{m\,s^{-1}}$) and interact with a wavy surface whose significant wave height H_s = 6.4 m. The primary variation between these simulations results from the wavy surface propagating at six different angles (0, 45, 90, 135, 180, -90)° relative to the direction of the geostrophic wind forcing. Bulk characteristics of these simulations can be found in the first six rows of Table 1.

Instantaneous wind fields: To gain an initial appreciation for the impact of the wavy surface's propagation direction, Fig. 8 presents instantaneous vertical slices of streamwise velocity for two simulations whose forcing is otherwise identical (*i.e.* U_g = 10 $\mathrm{m\,s^{-1}}$, H_s = 6.4 m), but the waves propagate at $\theta = 0°$ and 180°. Compared to $\theta = 0°$, flow over winds/waves with $\theta = 180°$ reveals notably lower streamwise velocity throughout the atmospheric boundary layer (ABL) with much larger horizontal variability. Statistics quantifying these variations and a discussion of the mechanisms producing these variations follows shortly.

Atmospheric boundary layer depth: The ABL is generally defined as: "The bottom layer of the troposphere that is in contact with the surface of the earth" (*e.g.,* Stull, 1988). The depth of the ABL represents an integral measure of all the turbulent motions produced/dissipated in the ABL

Imposed				Result							
U_g ($\mathrm{m\,s^{-1}}$)	H_s (m)	θ (°)	$\partial T_s/\partial t$ ($\mathrm{K\,h^{-1}}$)	w_{age}	ϕ (°)	U_{10} ($\mathrm{m\,s^{-1}}$)	u_* ($\mathrm{m\,s^{-1}}$)	τ_{p_x}/u_*^2	τ_{p_y}/u_*^2	z_i (m)	z_i/L
10	6.4	0	0	2.99	15.5	6.02	0.22	0.009	-0.018	301.0	0.30
10	6.4	45	0	2.97	27.5	6.06	0.22	-0.132	0.039	300.6	0.30
10	6.4	90	0	2.95	68.0	6.10	0.25	-0.051	0.108	306.1	0.31
10	6.4	135	0	3.23	108.3	5.58	0.33	-0.117	0.073	318.1	0.32
10	6.4	180	0	3.85	160.0	4.68	0.39	-0.136	-0.008	333.4	0.33
10	6.4	-90	0	3.28	95.1	5.49	0.29	-0.040	-0.143	305.1	0.31
10	2.9	0	0	1.97	16.7	6.10	0.23	-0.017	-0.008	309.4	0.31
10	2.9	45	0	1.96	27.2	6.13	0.23	-0.017	0.002	309.5	0.31
10	2.9	90	0	1.95	68.5	6.15	0.24	-0.028	0.044	315.2	0.32
10	2.9	135	0	2.13	108.4	5.64	0.29	-0.073	0.044	323.4	0.32
10	2.9	180	0	2.47	158.0	4.87	0.34	-0.094	-0.006	334.8	0.34
10	2.9	-90	0	2.15	98.6	5.57	0.27	-0.024	-0.082	313.0	0.31
10	0.7	0	0	0.97	18.4	6.18	0.23	-0.006	-0.001	317.6	0.32
10	0.7	45	0	0.97	26.8	6.21	0.23	-0.005	-0.003	317.8	0.32
10	0.7	90	0	0.96	70.1	6.26	0.23	-0.003	0.001	318.3	0.32
10	0.7	135	0	0.99	112.1	6.02	0.25	-0.009	0.006	324.1	0.32
10	0.7	180	0	1.08	158.9	5.54	0.28	-0.014	-0.001	332.2	0.33
10	0.7	-90	0	1.02	104.5	5.91	0.24	-0.003	-0.009	317.8	0.32
5	6.4	0	0	2.99	15.5	6.02	0.22	0.009	-0.018	301.0	0.21
5	6.4	45	0	2.97	27.5	6.06	0.22	-0.132	0.039	300.6	0.21
5	6.4	90	0	2.95	68.0	6.10	0.25	-0.051	0.108	306.1	0.21
5	6.4	135	0	3.23	108.3	5.58	0.33	-0.117	0.073	318.1	0.22
5	6.4	180	0	3.85	160.0	4.68	0.39	-0.136	-0.008	333.4	0.23
5	6.4	-90	0	3.28	95.1	5.49	0.29	-0.040	-0.143	305.1	0.21
10	6.4	0	0.25	2.84	21.5	6.34	0.18	0.018	-0.038	185.4	4.09
10	6.4	90	0.25	2.78	59.5	6.47	0.21	-0.077	0.115	188.1	3.47
10	6.4	180	0.25	4.86	135.0	3.71	0.30	-0.183	-0.018	213.8	7.65
10	6.4	-90	0.25	3.82	93.3	4.71	0.23	-0.056	-0.218	185.6	4.72

Table 1: Table outlining key characteristics of the large-eddy simulation cases under investigation. The significant wave height H_s is calculated as $4\sigma_h$. θ is the wave propagation angle relative to the geostrophic wind U_g in degrees °. $\partial T_s/\partial t$ is the imposed surface cooling rate. w_{age} is the wave age calculated as c_p/U_{10} where $U_{10} = (\langle u\rangle^2 + \langle v\rangle^2)^{1/2}$ evaluated at 10 m. ϕ is the absolute value of the relative angle between the wind direction at 10 m and the propagation direction of the waves for each simulation. $u_* = (\langle \tau_{T_x}\rangle^2 + \langle \tau_{T_y}\rangle^2)^{1/4}$ which is the square root of the total momentum stress evaluated at 10 m (see Eq. 3). τ_{p_x} and τ_{p_y} represent the contribution of pressure drag $\langle p\zeta_x/J\rangle$ and $\langle p\zeta_y/J\rangle$ to the total momentum stress at 10 m, respectively, where ζ_x and ζ_y are the grid transformation metrics and J is the Jacobian. z_i is the horizontal- and time-averaged boundary layer depth defined as the height of the maximum potential temperature gradient. L is the Monin-Obukhov length evaluated at 10 m.

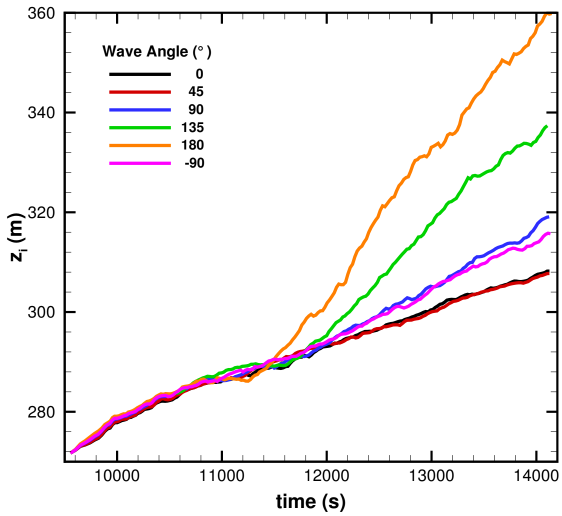

Figure 9: Time evolution of the depth of the boundary layer (z_i) in response to swell (H_s = 6.4 m) propagating at specified angles (wave angle, °) relative to the imposed geostrophic wind forcing ($[U_g, V_g]$ = [10, 0] $\mathrm{m\,s^{-1}}$). For all cases, the waves begin to grow into the domain at 9555.46 s of simulated time and are at full amplitude 400 s later. Note that after ~1500-2000 s, the winds finally come into equilibrium with the underlying wavy surface as exhibited by the nearly constant boundary layer growth rates that differ by wave angle.

through interactions with the surface. Therefore, evolution of the ABL depth occurring under variations in a single parameter illustrate that parameter's bulk influence on ABL turbulence.

Following Sullivan et al. (1998) and Davis et al. (2000), the ABL depth can be determined by searching vertically at every instant in time and at every horizontal grid point for the height of the maximum vertical temperature gradient. Following this search, one obtains height of the undulating surface coincident with the temperature inversion constraining ABL motions which can then be horizontally averaged to determine the average ABL depth at any instant in time. Time series of the instantaneous horizontally-averaged ABL depth (Fig. 9) reveals that the wave-propagation direction influences the ABL growth rate.

Starting at wave-propagation directions between 45° and 90°, the ABL grows faster than for the case where the waves propagate in the same direction as the driving pressure gradient (*i.e.* 0°). The ABL growth rate increases in a methodical fashion toward a maximum growth rate when the waves propagate in the opposite direction of the pressure gradient (*i.e.* 180°). The ABL growth rate responds similarly to waves propagating at ±90°. The mechanisms responsible for the ABL growth rates will be discussed shortly. Because the boundary layer grows at different rates across the simulations, all time-averaged statistics (where the averaging includes all times after 12000 s of simulated time) presented subsequently will be averaged into a time-evolving vertical coordinate system scaled by the instantaneous horizontally-averaged z_i.

Mean wind profiles: For these near-neutral* simulations, intercomparisons of the mean wind fields reveal that the direction of swell propagation significantly affects horizontally- and time-averaged wind speeds to heights all the way through the ABL (Fig. 10). For a fixed pressure gradient forcing ($[U_g, V_g]$ = [10, 0] $\mathrm{m\,s^{-1}}$), resultant streamwise wind speeds ($\langle u \rangle$) increasingly diminish as the swell propagation direction steps from 0° to 90° to a maximum wind speed decrease at 180°. Lateral wind speeds ($\langle v \rangle$) increase as the wave-propagation angle rotates from 0° to 135°;

*We use the term *near-neutral* loosely. Even though there's no surface buoyancy flux, warm air is continually entrained at the top of the ABL making the flow *weakly stable*; see z_i/L in Table 1.

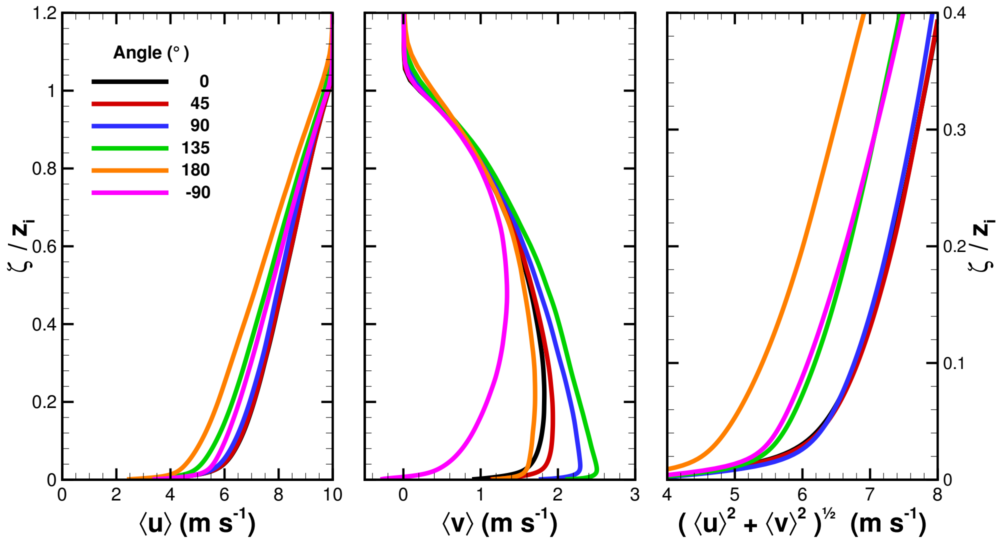

Figure 10: Vertical profiles of horizontally- and time-averaged wind aligned with the positive x-direction (left panel, $\langle u \rangle$) and the positive y-direction (middle panel, $\langle v \rangle$), and vector wind speed (right panel) in response to the wave-propagation angle (°) at heights (ζ) relative to the ABL depth (z_i). Note that the figures in the left and middle panels show the simulation results up to 1.2 times z_i, while the right-hand panel focuses in at the atmospheric region within which turbines operate (presuming a hub height of ~100 m and ~50 m turbine blades). Waves propagating opposite to the mean wind induce more pressure drag, thereby slowing down the wind in the predominant direction and increasing the turning of the wind via the Coriolis force.

$\langle v \rangle$ then decreases between 135° and 180°, and dramatically reduces in magnitude for the $-90°$-case as the swell generates near-surface winds in the negative y-direction.

Figure 10 shows that wave-propagation angles of ±90° reveal distinctly different wind profile responses resulting from the wave-induced pressure drag (Tab. 1) increasing to nearly twice the magnitude of the turbulent surface stress generating more Coriolis turning. Comparison of the mean $\langle u \rangle$ and $\langle v \rangle$ profiles suggests that the ABL's increased growth rate with increasing wave-angle (up to 180°) results from enhanced wave-induced pressure drag increasing the vertical shear (both in wind speed and direction) across the entrainment zone (*i.e.* at $\zeta/z_i \sim 1$). For the conditions simulated, the root-mean-square wind speed $(\langle u \rangle^2 + \langle v \rangle^2)^{1/2}$ reveals a 15% wind speed reduction at $\zeta/z_i = 0.3$ (~100 m) for the 180°-case compared to the 0°-case.

Turbulence: In an attempt to provide an overall measure of the influence of wave-propagation direction on turbulence levels relative to the mean wind speed, Figure 11 presents turbulence intensity profiles. Turbulence intensity is defined as:

$$TI = \frac{\left(\frac{1}{3}(\langle \sigma_u \rangle^2 + \langle \sigma_v \rangle^2 + \langle \sigma_w \rangle^2)\right)^{1/2}}{(\langle u^2 \rangle + \langle v^2 \rangle)^{1/2}} \tag{2}$$

where, $\sigma_{u,v,w}$ represents the standard deviation of each velocity component. Figure 11 shows that turbulence at hub-height ($\zeta/z_i \sim 0.3$) is more than a factor of two more intense when non-equilibrium surface waves propagate at 180° compared to when propagating at 0°. Table 1 suggests

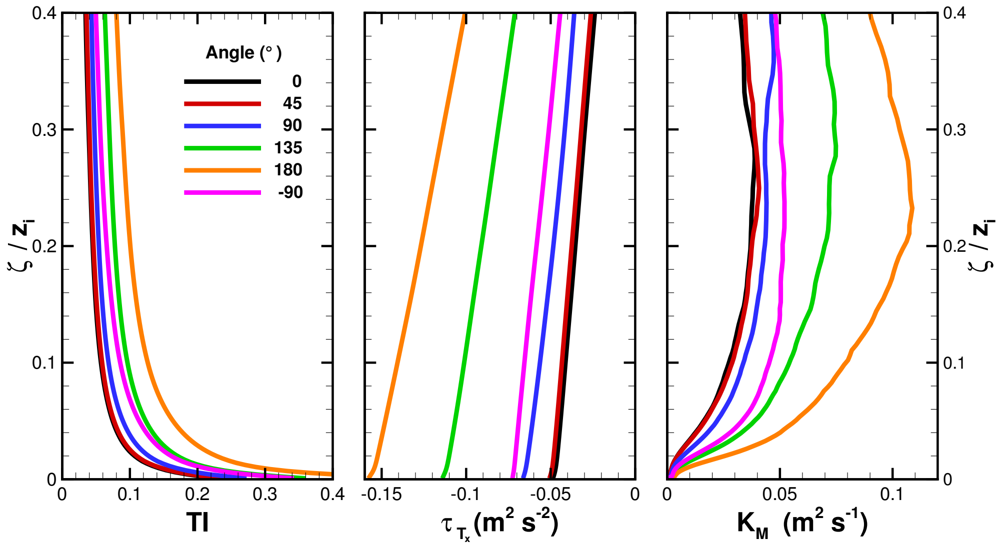

Figure 11: Vertical profiles of horizontally- and time-averaged TI, streamwise momentum stress τ_{T_x}, and the turbulent eddy diffusivity for momentum K_M in response to variations in the wave-propagation angle (°) at heights relative to the ABL depth (z_i).

that the surface friction velocity u_* increases by approximately eighty percent between the same two simulations. The middle panel of Fig. 11 presents the impact of the wave-induced increase in surface drag (increased u_*) on vertical profiles of the profile of the vertical momentum stress in the streamwise direction τ_{T_x}. τ_{T_x} is defined as:

$$\tau_{T_x} = \underbrace{\langle u'w' \rangle + \tau_{13}}_{\tau_t} + \underbrace{\langle p\,\zeta_x / J \rangle}_{\tau_p} \tag{3}$$

where τ_t is the sum of the turbulent momentum flux resolved by the LES plus the contribution from the subfilter-scale model, and τ_p represents the influence of asymmetries in the pressure field associated with the underlying surface wave field (*i.e.* the surface pressure drag). The wave-induced increase in the surface stress between the cases with 0° and 180° significantly increases the vertical gradient of τ_{T_x} as the surface demands a larger downward transport of momentum. As a result, the 180°-case produces approximately a three times larger momentum flux for a given vertical gradient of the mean horizontal wind speed ($K_M = -\tau_{T_x} / \frac{\partial u}{\partial \zeta}$).

4.3.5 Influence of wave age

Here, we investigate the influence of significant wave height ($H_s \sim 4\sigma_h$, where σ_h is the standard deviation of the surface wave height h) and wave propagation angle on the winds and turbulence. The objective of these simulations is to elucidate the atmospheric response to swell generated far away which is therefore likely misaligned with the mean wind.

Wave age is used as a parameter to characterize the wave propagation speed relative to the overlying atmospheric flow fields. As was discussed above when building the waves, wave age is defined as $w_{age} = c_p / U_{10}$, where c_p is imposed by the three different wavy surfaces, and U_{10} now represents the simulation-derived scalar wind speed at 10 m. For the simulations conducted, w_{age}

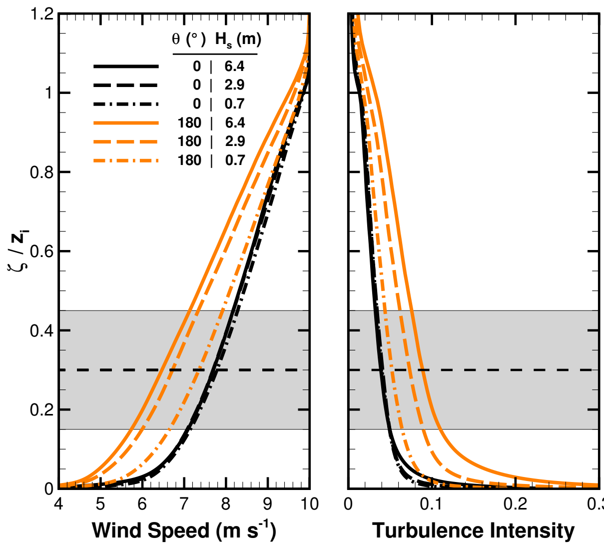

Figure 12: Vertical profiles of the horizontally- and time-averaged scalar wind speed ($\sqrt{\langle u^2 \rangle + \langle v^2 \rangle}$, left panel) and turbulence intensity (TI, right panel) in response to swell propagating at two specified angles ($\theta = 0°$ and $180°$) relative to the imposed geostrophic wind forcing and for the three significant wave heights H_s. The long-dashed line indicates approximately 100 m (the hub height of a typical turbine) and the shaded region indicates the vertical region spanning a representative rotor plane.

varies from 0.96 up to 3.85 (where $w_{age} = 1.2$ is generally classified as wind-wave equilibrium). Recently, it has been argued that w_{age} should incorporate the influence of the relative direction between U_{10} and the wave propagation direction (*e.g.,* Hanley et al., 2010); the angle between these two directions will be hereafter referred to as ϕ. However, to ease the interpretability of the current effort compared to previous work, Table 1 presents the traditional definition of w_{age} and ϕ separately. If one were to calculate the wave age associated with the component of the wind perpendicular to the primary propagation direction of the surface waves, *i.e.* replacing U_{10} with $U_{10}cos(\phi)$, the effective wave age for the current simulations would range from -37 to +8.

Surface drag and Coriolis turning: Inspection of Table 1 reveals that ϕ not only varies with θ, but also with variations in H_s. The momentum balance requires the imposed geostrophic wind [U_g, V_g], the Coriolis force, and the total surface drag to balance. Since [U_g, V_g] and the Coriolis parameter ($f = 1 \cdot 10^{-4}$ s^{-1}) are fixed across all simulations, ϕ variations with H_s are largely controlled by the magnitude variation in the surface drag. Note that for the case with $\theta = 0°$ where the waves are propagating in a direction nearly aligned the wind, waves with a large significant wave height ($H_s = 6.4$ m) induce less drag than do smaller, slower moving (lower c_p) waves. Cases with $w_{age} > 1.2$ (*i.e.* cases where the winds and waves are in disequilibrium) reveal increasing wave-induced pressure drag with increasing θ and/or ϕ. The pressure drag peaks when $\theta = 180°$ ($\phi \sim 160°$), with the total pressure drag ($\tau_p = \sqrt{\tau_{p_x}^2 + \tau_{p_y}^2}$) at 10 m contributing (13.6, 9.4, 1.4)% the momentum stress when H_s = (6.4, 2.9, 0.7), respectively.

Winds and turbulence: For these near-neutral (or slightly stable) simulations, intercomparison of the vertical profile of the scalar wind speed reveals that even for cases that are in near wind-wave equilibrium ($H_s = 0.7$, $w_{age} \sim 1$) the wave-induced pressure drag induced by waves propagating counter to the wind ($\theta = 180°$, $\phi \sim 160°$) is sufficient to reduce hub height wind speeds by nearly 4% compared to when the waves propagate with the wind ($\theta = 0°$, $\phi \sim 16°$); note that when

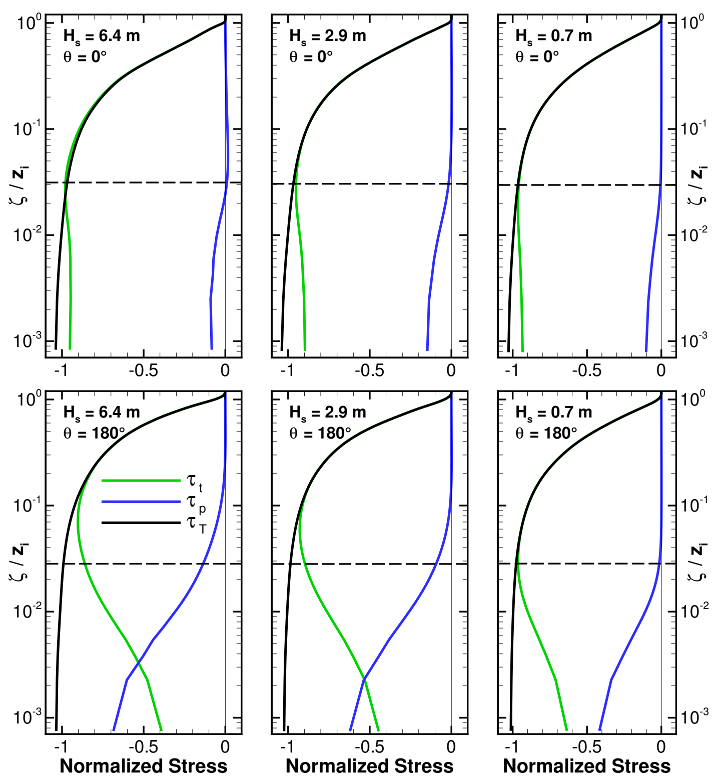

Figure 13: Vertical profiles of horizontally- and time-averaged total momentum stress in the streamwise direction (τ_T, solid black line) for the three different significant wave height H_s simulations and the simulations responding to the two extreme propagation angles of the surface waves θ = 0° and 180°. The colored lines depict the two components contributing to the total stress; the green line is the turbulent stress τ_t, and the blue line is the contribution from wave-induced asymmetries in the pressure field with respect to the undulating grid τ_p as defined in Eq. 3, although for simplicity we've left off the subscript x on each term. The profiles have been normalized by the total 10-m momentum stress u_*^2. The dashed line depicts the 10 m height. Note that these fields are generated by averaging in the wave-following coordinate system, *i.e.* along lines of constant ζ.

considering the same directional comparison for the situation where $H_s = 6.4$ ($w_{age} \sim 3$ to 4), hub height wind speeds decrease by as much as 15% (Fig. 12). Figure 12 also shows that the increased pressure drag induced by the waves when their propagation direction transitions from θ = 0° to θ = 180° increases hub-height turbulence intensity by factors of (1.3, 1.8, 2.3) for $H_s = (0.7, 2.9, 6.4)$ m, respectively.

For many years in the air-sea interaction community, it was presumed that 10 m is sufficiently high above the water surface to be above the direct influence of the waves (but still within the inertial sublayer where the turbulent momentum flux would be constant with height) such that turbulent fluxes or shearing stress measured at this height represent that occurring at the surface (Toba et al., 2001). Smedman et al. (1999) (among others) showed that depending upon the propagation speed of the waves relative to the wind speed (*i.e.* with increasing w_{age}), that the surface waves could be felt up to ∼200 m above the surface implying that observations taken at the 10 m reference height could be significantly impacted by the underlying surface. Figure 13 presents vertical profiles of the components contributing to the total horizontally- and time-averaged momentum stress τ_T in the streamwise direction x for the three different significant wave height H_s simulations and the two extreme propagation angles of the surface waves θ = 0° and 180°. The three solid lines in Fig. 13 are described in Eq. 3. When θ = 0°, increasing H_s (and subsequently increasing c_p), τ_p is generally small and negative near the surface. However the H_s = 6.4 case reveals that above 10 m, the wave-induced pressure field acts to accelerate the winds (*i.e.* swell-driven winds) as revealed through positive τ_p. When θ = 180°, both τ_t and τ_p remain negative through all heights, and τ_p generally increases with increasing H_s (and subsequently increasing c_p). Of importance to note

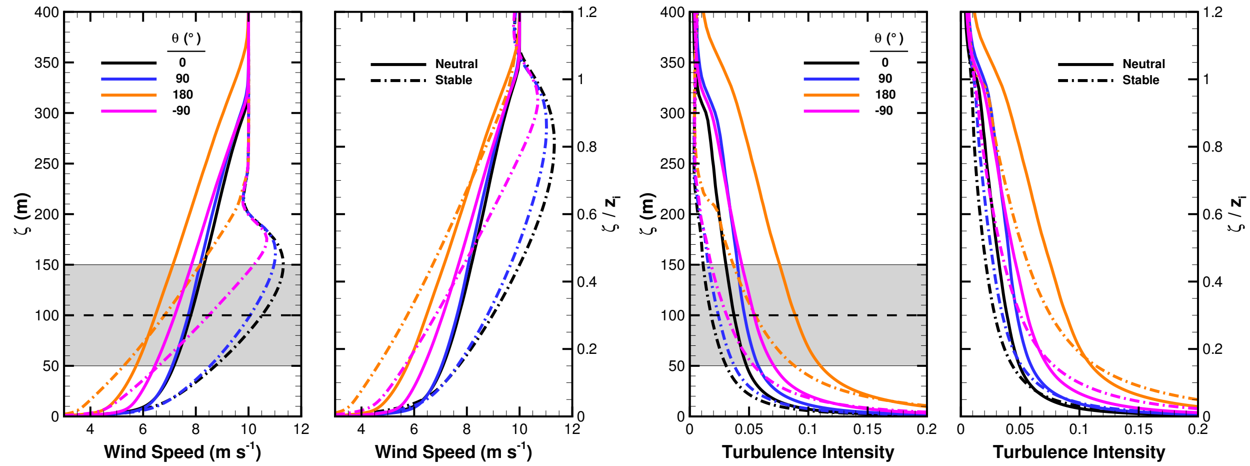

Figure 14: Vertical profiles of the horizontally- and time-averaged scalar wind speed ($\left[\langle u^2 \rangle + \langle v^2 \rangle\right]^{1/2}$, left two panels) and turbulence intensity (TI, right two panels) in response to swell propagating at four specified angles ($\theta = 0°$ (black), 90° (blue), 180° (orange), and -90° (pink)) relative to the imposed geostrophic wind forcing. For all cases, the significant wave height H_s is 6.4 m. Solid lines show the neutrally-stratified profiles and the dash-dot lines show profiles from the stably-stratified cases. The dashed line marks 100 m (the hub height of a typical turbine) and the shaded region indicates the vertical region spanning a representative rotor plane. Both wind speed and TI plots present the same data; where, the left panel displays the data in physical height above the water surface, and the right panel displays the data in height units scaled to the ABL depth (z_i).

is that for situations with θ = 180°, the 10-m turbulent momentum flux represents a decreasing portion of the total stress with increasing H_s; such that for the case with H_s = 6.4, τ_p contributes to nearly 20% of the downward momentum transport at 10 m and remains a substantial portion of that transport up beyond the height of the surface layer (traditionally presumed to be $z/z_i \sim 0.1$).

4.3.6 Influence of stability

Relative to neutral stratification, mean wind profiles in the stable cases generally develop a pronounced wind speed maxima (a jet, Fig. 14). The height of the jet varies with wave propagation direction relative to the geostrophic wind direction (θ). For aligned winds and waves ($\theta = 0°$) the jet occurs at a height of about $\zeta/z_i = 0.8$ and is about 15% larger in magnitude than the geostrophic wind speed. However, with the increasing drag induced by waves propagating at directions counter to the wind, the height at which the jet occurs shifts upward and the magnitude diminishes such that for the case of misaligned winds/waves ($\theta = 180°$) the jet completely disappears. The wind speed profiles for the stable cases (dash-dot lines) also exhibit substantially larger vertical shear compared to the neutral cases; this shear increases with increasing wind/wave misalignment.

Near the surface, this enhanced shear increases near-surface turbulence intensity (Fig. 14, right two panels), however turbulence intensity at hub-height (dashed line) diminishes between the neutral and stratified cases as a result of buoyant destruction such that the stable cases all reveal lower turbulence intensities above hub height than do the neutral cases.

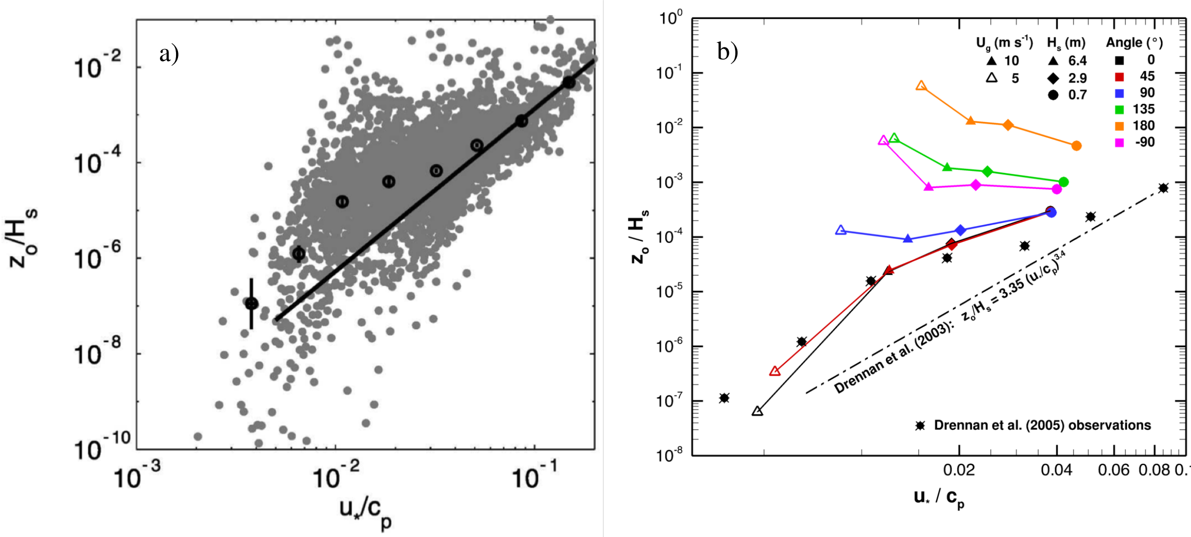

Figure 15: a) Non-dimensional surface roughness $z_\circ/H_s$ as a function of inverse wave age, u_*/c_p from seven different offshore field campaigns (from: Drennan et al., 2005). H_s is significant wave height and c_p is the phase speed of the peak in the wave spectrum. The black open circles represent are bin-averaged means, and the error bars represent two standard errors about the mean. The solid black line depicts the Drennan et al. (2003) curve (Eq. 4). b) Non-dimensional surface roughness $z_\circ/H_s$, as a function of inverse wave age, u_*/c_p. The neutrally-stratified LES results are separated by wave propagation angle relative to the wind direction (marked by color). Each of these angles is presented for three different significant wave heights H_s and for a geostrophic wind of 10 m s^{-1}. For the largest waves (H_s = 6.4 m), the open symbols represent LES results for a geostrophic wind of 5 m s^{-1}. The colored lines connect LES results for similar wave-propagation-direction angles relative to U_g. The black diamond symbol with an $\times$ through it depicts Drennan et al.'s (2005) bin-averaged observations. Drennan et al.'s (2003) parameterization is presented in the black dash-dot line.

4.4 Parameterization

4.4.1 Non-dimensional surface roughness

Previous research (*e.g.,* Drennan et al., 2003, 2005) has suggested the following variation of $z_\circ$ normalized by the significant wave height H_s and inverse wave age (defined as: $w_{age}^{-1} = u_*/c_p$):

$$\frac{z_\circ}{H_s} = 3.35\left(\frac{u_*}{c_p}\right)^{3.4}. \qquad (4)$$

Observations from a number of offshore experiments agree with their formulation for young waves and up to approximately wind-wave equilibrium (w_{age} ~30), see Fig. 15a. For swell, or old waves (left side of Fig. 15a), the data exhibits significant scatter and the bin-averaged mean $z_\circ/H_s$ deviates positively from what Eq. 4 would predict.

To elucidate the mechanisms responsible for the observed scatter in $z_\circ/H_s$ when waves are old (swell), we now lay our neutrally-stratified LES results over top of Drennan et al.'s (2003; 2005) bin-averaged data and parameterization (Fig. 15b). Here, the LES-derived $z_\circ$ is calculated based upon winds U_{10} and friction velocity $u_{*_{10}}$ averaged along a coordinate line 10-m above the water

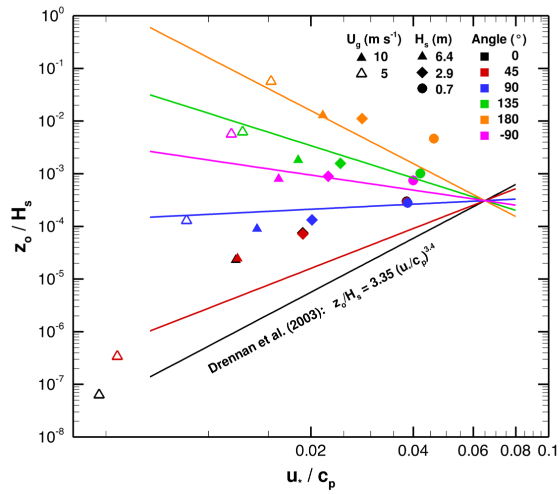

Figure 16: Non-dimensional surface roughness $z_\circ/H_s$, as a function of inverse wave age, u_*/c_p from the neutrally-stratified LES (colored symbols, which are described in Fig. 15). The black line depicts Drennan et al.'s (2003) parameterization. The colored lines represent the results of our modification to Drennan et al.'s (2003) form, and which is presented in Eq. 6.

surface, via:

$$z_\circ = 10 \exp\left(\frac{U_{10}\,\kappa}{u_{*10}}\right). \tag{5}$$

The LES results compare extremely well with Drennan et al.'s (2003; 2005) data (compare Figs. 15a and 15b, using the bin-averaged Drennan et al. (2005) data as a reference). Importantly, the LES results suggest that the variability of $z_\circ/H_s$ at large w_{age} discussed by (Drennan et al., 2005) can largely be explained by incorporating the propagation direction of the waves (*i.e.* reduced $z_\circ$ when swell propagates with the waves, and incrementally increasing $z_\circ$ as the waves transition to propagate at directions counter to the driving pressure gradient, peaking at 180°, and reducing again at $-90°$). The relatively large $z_\circ$ values for the lower wind speed cases (open triangles) with waves propagating at directions different to U_g should be taken with some caution since outdoors the small waves that carry much of the drag (Sullivan et al., 2014) would dissipate semi-rapidly – a feature which we can not reproduce here because our waves are imposed and are therefore unable to respond to the overlying wind field.

In an attempt to incorporate wave propagation direction influences within Drennan et al.'s (2003) parameterization (Eq. 4), we developed the following expression:

$$\frac{z_\circ}{H_s} = A\left(\frac{u_*}{c_p}\right)^{3.4\,cos(0.94\,\phi)}, \tag{6}$$

where, ϕ is the angle between U_{10} and the wave propagation direction, and A is an adjustable parameter. Figure 16 compares predictions using Eq. 6 against the LES data, where the value of A is chosen for each ϕ such that the prediction of $z_\circ/H_s$ matches Drennan et al.'s (2003) form when inverse wave age u_*/c_p = 0.065. The modified form presented Eq. 6 captures the wave-direction-induced variation in the LES results reasonably well. However it should be noted that in practice, this parameterization will require a technique to limit $z_\circ$ so that the predicted $z_\circ$ does not extend beyond the envelope containing the observed data at low inverse wave age.

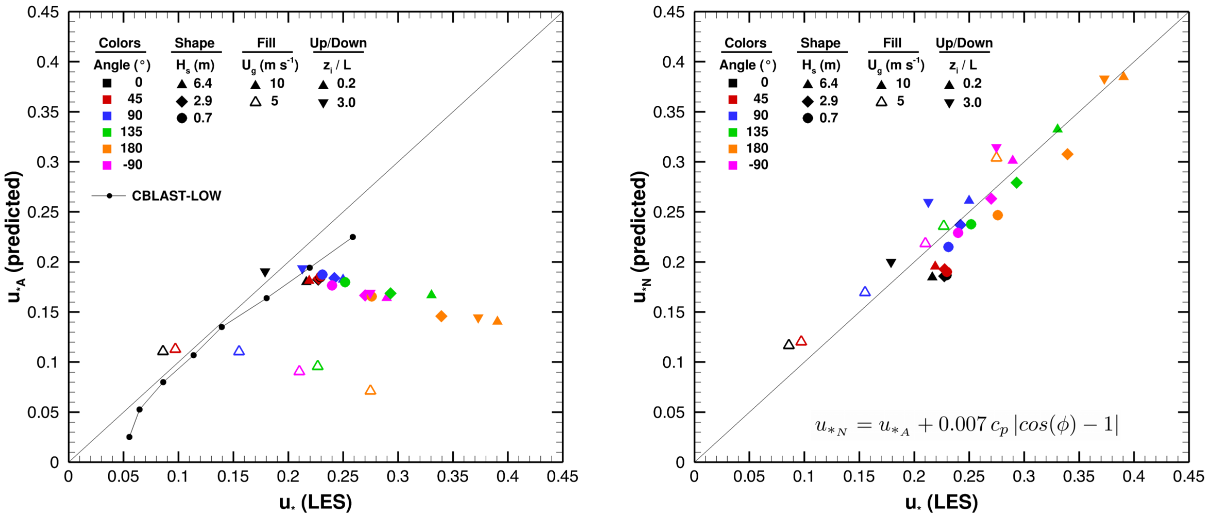

Figure 17: Left) Predictions of u_* using U_{10} in Eq. 7 from each of the LES runs compared to the 10-m u_* from the LES and observations from CBLAST-Low under neutral conditions (small black dots connected by lines). Note that because Eq. 7 comes from Andreas et al. (2012), this panel uses the terminology that the predicted u_* is called u_{*_A}. The symbol colors, shape, and fill are the same as those discussed in Fig. 15, however in this figure the stable cases for U_g = 10 m s^{-1} and H_s = 6.4 m are included as downward triangles. Right) Predictions of u_* using U_{10} in Eq. 8 from each of the LES runs compared to the 10-m u_* from the LES. u_{*_A} is predicted using Eq. 7. The symbol colors, shape, and fill are the same as those discussed in Fig. 15, however in this figure the stable cases for U_g = 10 m s^{-1} and H_s = 6.4 m are included as downward triangles.

4.4.2 Direct relationship between u_* and U_{10}

Andreas et al. (2012) presented a technique to account for wave-state influences on the relationships between the 10-m wind U_{10} and the drag of the underlying surface (characterized by u_*). In their formulation, Andreas et al. (2012) abandoned MOST and found that the following direct relationship:

$$u_* = 0.239 + 0.0433\left[(U_{10} - 8.271) + [0.120(U_{10} - 8.271)^2 + 0.181]^{1/2}\right] \tag{7}$$

reproduces data from ten different offshore field campaigns.

Andreas et al.'s (2012) relationship (Eq. 7) works reasonably well for the LES data when the waves are nearly-aligned with the mean pressure gradient (red and black symbols, Fig. 17); although we do not have access to wave-state information for CBLAST-Low, the trends in the CBLAST-Low data reflect a similar character to that found in the LES. Eq. 7 dramatically under predicts u_* compared to the LES when the waves propagate at large angles relative to the wind direction (left panel, Fig. 17); a finding which Andreas et al. (2012) were only able to hint at with their observations. If we refer to u_* in Eq. 7 as u_{*_A}, using the LES data we can alter u_{*_A} to account for the influence of swell propagation direction using:

$$u_{*_N} = u_{*_A} + 0.007\, c_p\, |cos(\phi) - 1| \ , \tag{8}$$

where, c_p is the phase speed of the peak in the surface wave spectrum and ϕ is the angle between the 10-m wind direction and the propagation direction of the surface waves. Using the LES-derived U_{10} values to estimate u_* via Eq. 8 substantially collapses the predictions along the one-to-one line as compared with the LES-calculated u_* values (right panel, Fig. 17); even the stable cases fit this formulation (downward pointing triangles). That said, we're not 100% happy with the formulation presented in Eq. 8 because it is 'additive', but Eq. 8 clearly improves Andreas et al.'s (2012) formulation (Eq. 7) by incorporating the phase speed of the waves c_p and their propagation direction ϕ.

4.4.3 Roughness modifications for shallow water

Jiménez and Dudhia (2015) have found from evaluating deep-water formulations in WRF at FINO1 that high-wind biases exist that can be systematically 10% too high at wind speeds up to 20 $\mathrm{m\,s^{-1}}$. This is attributable to the wave-shortening and steepening effect of shallow water that consequently leads to increased drag for a given wind speed. The water depth at FINO1 is ~30m, and is in the range where an effect of this magnitude has been hypothesized by Taylor and Yelland (2001) from previous shallow-water field data. Jiménez and Dudhia (2015) were able to correct the wind bias by fitting a new roughness length formulation as a function of wind speed using 1 year of tower data in 2009 and model simulations of the whole period. The new formulation gives significantly higher 10-m drag coefficients that even exceed $C_d = 0.003$ at 20 $\mathrm{m\,s^{-1}}$, and this is consistent with previous field-derived estimates from eddy covariance measurements. Deep-water formulations commonly used in models such as Edson et al. (2013) and the traditional Charnock formulation have 30-40% lower drags at these wind speeds. This includes the Andreas et al. (2012) formulation that was also largely based on deep-water measurements. This work points to a need to consider modified roughness length formulations based on water depth for shallow regions, which is highly relevant to wind-farm locations.

4.5 Implementation in WRF

4.5.1 WRF-SCM simulations

No wave effects: Before running full three-dimensional simulations with the WRF model, we carried out numerical simulations using WRF Single Column Model (WRF-SCM) implementation. WRF-SCM is a complete version of WRF, but run on a 2×2 horizontal grid (Fig. 18) with periodic boundary conditions thereby permitting rapid testing of WRF physics.

Initial and boundary conditions for the WRF-SCM simulations were derived using global data from NOAA's Climate Forecast System Reanalysis (CFSR, Saha, 2010). The global CFSR data are available on a 0.5 degree grid at six-hour intervals and cover a time period between 1979 and 2010. Sea surface temperature data were obtained from National Center for Environmental Prediction (NCEP)'s Optimum Interpolation Sea Surface Temperature (OISST) project available on a 1/12 degree grid for year 2006. We use the MYNN 2.5 level PBL scheme for all WRF-SCM simulations (Nakanishi and Niino, 2004, 2006).

A WRF-SCM simulation was carried out for the month of October 2006 focusing on the FINO1 platform location (N 54°0′53.5″ E 6°35′15.5″). Two time periods (October 7 and October 27-28) were selected because the wind direction was nearly identical while the wave propagation direction

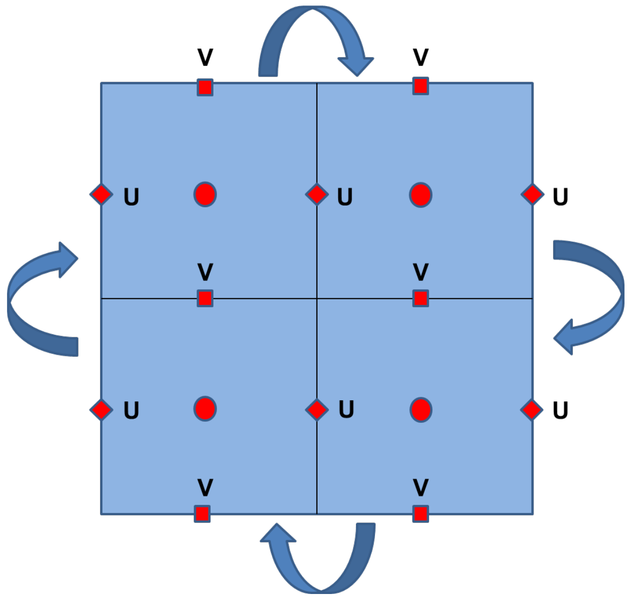

Figure 18: Schematic diagram of the WRF-SCM horizontal grid consisting of 2×2 grid cells with periodic boundary conditions.

was nearly opposite. Furthermore, in both cases significant wind speeds in the operational range of a modern off-shore wind turbine and significant wave heights were observed. These cases are therefore suitable for further analysis of the effects of waves on hub-height winds.

WRF-SCM simulation results were compared with observations with intent to assess their accuracy with attention to the ability of the PBL scheme to accurately represent the lower levels of a marine boundary layer. The attempt is made to identify the effects of waves propagating at different angles with respect to the wind direction on the wind speed profile.

Wind speed profiles for two selected time periods in October 2006 are shown in Fig. 19 where the wind speed profiles at six-hour intervals are presented. One can observe that during October 7 (Fig. 19, left panel) when the wave direction is nearly opposite to the wind direction the wind speed, there is significant vertical shear of the horizontal wind speeds from the sea surface up to 100 m. In contrast, between October 27 and 28 when the winds and waves were nearly aligned, wind speed is essentially independent on the height above sea level (Fig. 19, right panel).

While WRF-SCM simulations in both cases capture the general shape and evolution of wind profiles including speedups and slowdowns, there are significant differences in wind speed magnitude between simulated and observed wind profiles. The differences in wind speed magnitudes, can largely be attributed to uncertainties in initial and boundary conditions, among other causes. However, consistent with the LES results, when waves propagate in a direction opposite to the wind direction, the wind profiles exhibit higher near-surface shear compared to the case when waves are not present – presumably resulting from the additional wave-induced drag. Alternatively, when waves propagate in the same direction as the wind, wind speed shear levels reduce in comparison. Notice that on October 27 wind speed profile exhibits negative shear above 70 m; this feature is also consistent with possible effect of waves propagating in the direction aligned with the wind – effectively exerting negative drag (accelerating the wind in the lowest layers).

With wave effects: Since our parameterization hinges on Andreas et al.'s (2012) relationship between U_{10} and u_* in the surface layer (Eq. 7), we first needed to include Andreas et al. (2012) as

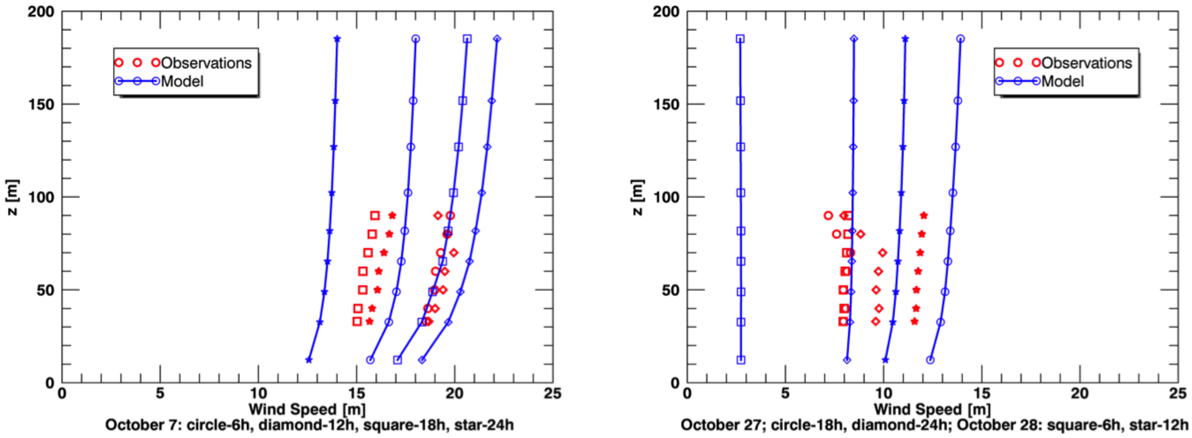

Figure 19: Wind speed profiles on October 7, 2006 (left) and October 27-28, 2006 (right) on the FINO1 tower. Observations (red) and WRF-SCM predictions (blue). One-hour-averaged profiles are presented at six-hourly intervals (symbols).

an option within WRF's MYNN model. We were then able to incorporate our wave-state modification to Andreas et al. (2012) (Eq. 7) as well. Once these new formulations were introduced into the MYNN model, we tested them against observational data from the FINO1 tower.

We modified WRF so that it reads variables describing the wave-state which were derived from the FINO1 observations. These variables include: 1) significant wave height, 2) wave period, and 3) wave propagation direction. Data derived from the NCEP Final Operational Global Analysis data set were used to drive the simulations. Geostrophic forcing and advection tendencies were extracted from the NCEP analysis data as well as initial profiles of the wind velocity components, potential temperature and humidity. The WRF-SCM simulations were performed for the same month of October 2006, initial conditions, and forcings as discussed above.

Figure 20a shows a comparison of predictions of wind speed at 90 m from the three WRF-SCM cases (Charnock, SCM-C; Andreas, SCM-A; and our new formulation, SCM-A-wave) against the FINO1 tower observations for the entire month of October 2006. The times at which the simulations are reset to the NCEP analysis data are apparent as obvious jumps in the data. Periods when the observed winds are suspected to be compromised by tower-shadowing have been eliminated. Surprisingly, the SCM-C (blue) and SCM-A (green) do not differ much, even though the surface layer treatment differs significantly and SCM-A presumes neutral stability. Differences between the SCM-A (green) and SCM-A-wave (red) are more noticeable and reflect the influence of our new wave-state parameterization. There are times that the new wave-state parameterization degrades the 90-m wind-speed prediction, and times that it improves the prediction. Generally the times when the predictions are improved coincide with times when the winds and waves are misaligned (not shown). Compared with the FINO1 data, the mean absolute error (MAE) are: 1.68 m s^{-1} for SCM-C, 1.70 m s^{-1} for SCM-A, and 1.79 m s^{-1} for SCM-A-wave.

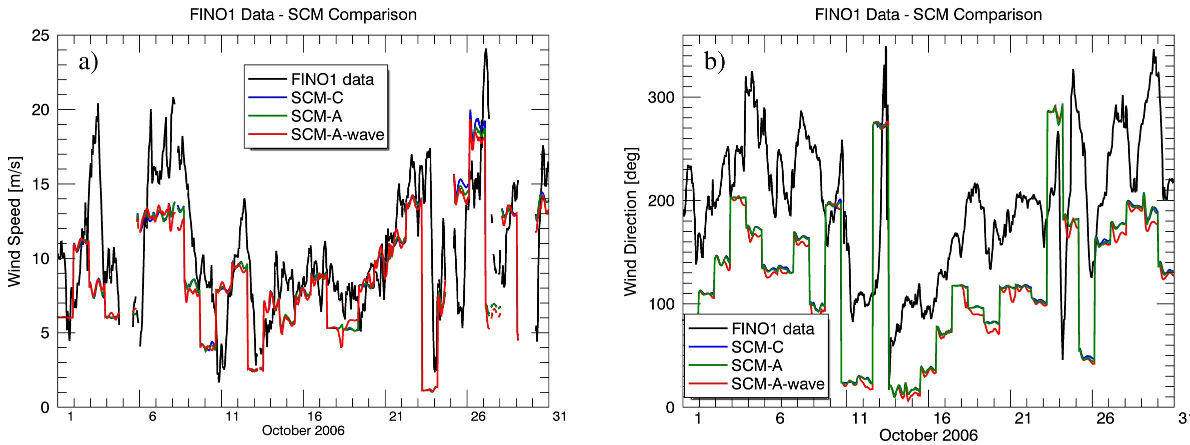

Figure 20: Time evolution of the 90 m wind speed (a) and wind direction (b) at FINO1 for the month of October 2006. The four lines presented are: 1) FINO1 observations (black), 2) WRF-SCM results using the Charnock (1955) surface-layer parameterization (blue, SCM-C), 3) WRF-SCM results using the Andreas et al. (2012) surface-layer parameterization (green, SCM-A) according to Eq. 7, and 4) WRF-SCM results using the Andreas et al. (2012) surface-layer parameterization modified for wave-state influences according to (red, SCM-A-wave) according to Eq. 8. The WRF-SCM simulations are driven by NCEP's Global Reanalysis data updated at midnight each day during the month-long simulation. To eliminate any issues associated with tower-shadowing, periods when the winds are from between 280° and 340° are not included.

4.5.2 3D WRF simulations

Following the successful test of our new surface layer formulation accounting for the effects of swell implemented within WRF-SCM, we used a three-dimensional, limited area version of WRF V3.6.1 to simulate an entire year (2006) over the North Sea. The numerical simulations were set up following Vestas' standard practices for wind resource assessment. Each simulation was carried daily for 30 hours starting at 00h UTC. The first 6 hours were used as a spin-up period. The output was saved every 20 minutes for 24 hours between 06h UTC on the first day and 06h UTC on the second day. The computational domain covered the North Sea and North-Eastern Europe centered on the FINO1 tower and was discretized using nested computational domains with grid cell sizes of 9 km, 3 km, and 1 km. The innermost domain covered an area of 100 km $\times$ 100 km. In the vertical direction we used a stretched grid with 37 levels. Initial and boundary conditions were derived from NCEP's Final Operational Global Analysis.

To assess the influence of the new parameterization, we carried out two simulations. A baseline simulation used WRF's standard Charnock parameterization of wave effects on all domains, while the second simulation includes our new surface layer parameterization on the innermost domain only and used the Charnock parameterization on the outer domains. The assumption is that the wave state in the broad area surrounding the FINO1 tower can be represented by the measurements at the tower. In the simulation including the influence of waves, observed wave-state information from FINO1 was updated hourly and held constant for the subsequent hour.

Results of the two three-dimensional WRF simulations are shown in Fig. 21. Annually averaged wind speed measurements at the FINO1 tower are presented with red diamonds, the green dashed line denotes simulation results with Charnock parameterization on all domains, and the

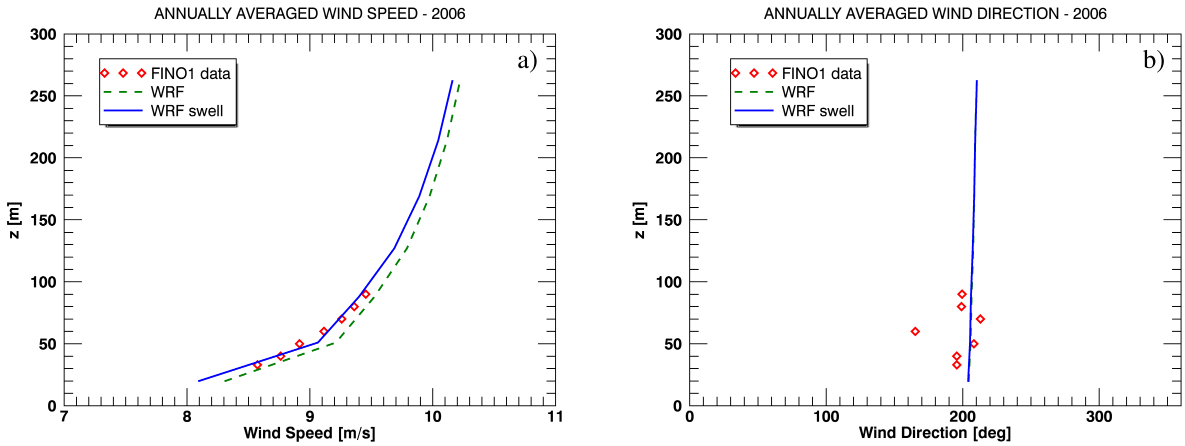

Figure 21: Vertical profiles of annually averaged: (a) wind speed, and (b) wind direction at the FINO1 tower for 2006. Red diamonds depict the FINO1 tower observations, the green dashed line depicts results from a 3D WRF simulation using WRF's traditional Charnock formulation for $z_\circ$, and the solid blue line depicts results from a 3D WRF simulation where the surface friction velocity is determined using Eq. 8 using the observed hourly wave data at FINO1.

solid blue line denotes three-dimensional WRF results with the new parameterization accounting for the effects of non-equilibrium waves on the innermost domain. Although the differences between two WRF simulations are relatively small (Fig. 21a), better agreement between the observations and the simulation accounting for the effect of swell is noticeable. During 2006 at FINO1, winds and waves were generally misaligned (see Fig. 5). Therefore, when incorporating wave influences into the simulations, the increased drag induced by swell propagating at directions counter to the winds should act to increase the surface drag and reduce wind speeds; Figure 21a reveals that the wave-state parameterization has precisely this influence on the annually-averaged wind profile predictions. The simulated wind direction in both WRF simulations direction is generally in good agreement with the data (Fig. 21b). Using the new surface layer parameterization MAE in hub height winds (at 91 m) reduces from 2.81 $\mathrm{m\,s^{-1}}$ to 2.77 $\mathrm{m\,s^{-1}}$, while the root mean square error (RMSE) is reduces from 3.60 $\mathrm{m\,s^{-1}}$ to 3.54 $\mathrm{m\,s^{-1}}$. These annually-averaged error reductions are relatively modest, but certainly reflect increased skill.

The effects of our new parameterization are more significant when specific cases are considered. In Fig. 22, observed and simulated wind speed are shown for two different days, October 9 and November 13, 2006. On October 9, the angle between the observed wind direction and the wave-propagation direction was 180° (opposite) and the wave height 1.3 m. On November 13 the angle between the observed winds and waves was 60° (nearly-aligned) and the wave height 3 m. Waves opposing the winds increases the surface drag reducing predicted hub-height wind speeds (Fig. 22a); when waves are aligned with the winds (Fig. 22b), wave-induced surface drag accelerates the wind. In both cases, the simulation accounting for non-equilibrium winds/waves results in significantly better agreement with the observations with hub height wind speed differences between the two simulations of about 1 $\mathrm{m\,s^{-1}}$.

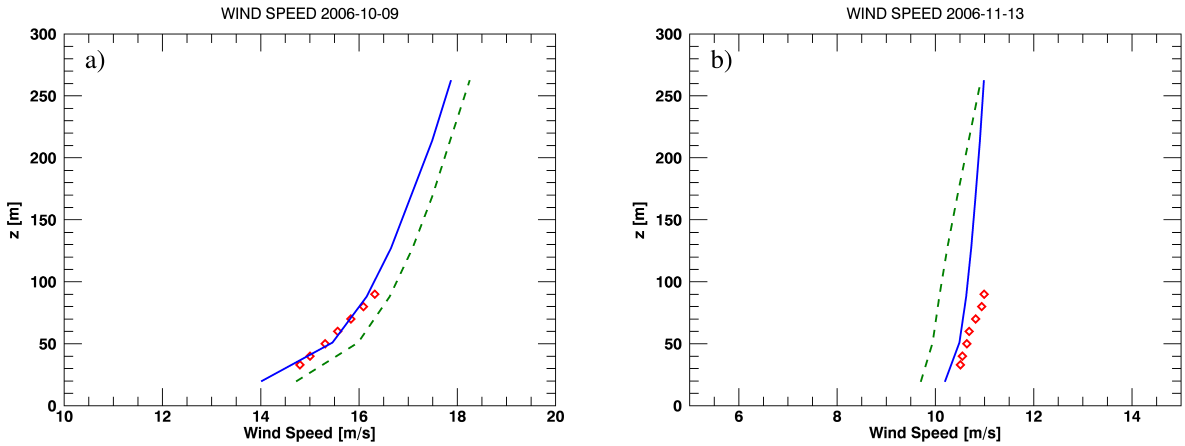

Figure 22: Comparison of simulations and observations of the wind speed at FINO1 on: (a) October 9, 2006, and (b) November 13, 2006. Symbols represent observations and lines simulation results as in Fig. 21. October 9, 2006 reflects a day when swell propagated in a direction opposing the winds, and November 13, 2006 reflects a day when winds and waves were nearly aligned.

5. Accomplishments

- Manuscripts published:
  1. Mahrt, L., D. Vickers, E. L. Andreas, 2014: Low-level wind maxima and structure of the stably stratified boundary layer in the coastal zone, *J. Appl. Meteor. Climatol.*, **53**, 363-376, doi: 10.1175/JAMC-D-13-0170.1
  2. Sullivan, P. P., J. C. McWilliams, E. G. Patton, 2014: Large-eddy simulation of marine atmospheric boundary layers above a spectrum of moving waves, *J. Atmos. Sci.*, **71**, 4001-4027, doi: 10.1175/JAS-D-14-0095.1
  3. Jiménez, P. A., J. Dudhia, 2015: On the wind stress formulation over shallow waters in atmospheric models, *Geosci. Model Dev. Discuss.*, **7**, 9063-9077, doi: 10.5194/gmdd-7-9063-2014, **submitted**
  4. Mahrt, L., E. L. Andreas, J. Edson, D. Vickers, J. Sun, E. G. Patton, 2015: Coastal zone surface stress with stable stratification, *J. Phys. Oceanogr.*, **submitted**
  5. Patton, E. G., P. P. Sullivan, B. Kosović, J. Dudhia, L. Mahrt, M. Žagar, L. Gulstad, 2015: On the influence of swell propagation-angle on surface drag, **in preparation for:** *J. Atmos. Sci.*

- Presentations given:
  1. Kosović et al., 2012: American Wind Energy Association Offshore Wind, Virginia Beach, VA
  2. Kosović et al., 2013: North American Wind Energy Academy Symposium, Boulder, CO
  3. Žagar et al., 2013: European Wind Energy Association Offshore Conference, Frankfurt, Germany

4. Patton et al., 2013: International Conference on Future Technologies for Wind Energy, Laramie, WY
5. Patton et al., 2014: American Meteorological Society's 21st Symposium on Boundary Layers and Turbulence, Leeds, United Kingdom
6. Patton et al., 2014: U.S. Department of Energy, Office of Energy Efficiency and Renewable Energy's Wind Power Technology Office Review, Arlington, VA
7. Mahrt et al., 2015: American Meteorological Society's 19th Conference on Air-Sea Interaction, Phoenix, AZ
8. Patton et al., 2015: Risø National Laboratory, Technical University of Denmark, Risø, Denmark

- Additional products:
  1. Analyzed observational data sets
  2. Data sets from idealized turbulence resolving simulations
  3. Wave-state sensitive surface drag parameterization has been submitted for inclusion in the next WRF release (v3.8).

6. Conclusions

6.1 Importance of Wave State

For fast moving swell (H_s = 6.4 m, c_p = 18 m s^{-1}), the boundary layer grows more rapidly when waves propagate opposite to the waves ($\theta = 180^\circ$) compared to when winds and waves are aligned ($\theta = 0^\circ$); with maximum entrainment rates at 180° resulting from enhanced vertical shear in both wind speed and direction across the entrainment zone. Misaligned winds/waves increase the surface pressure drag by nearly a factor of 2 relative to the turbulent stress for the extreme case where waves propagate at 180° compared to the pressure gradient forcing. Hub-height wind speeds reduce by nearly 15% for the 180°-case compared to the 0°-case, and turbulence intensities increase by nearly a factor of 2 – information that will help manufacturers design/deploy turbines that are suitable for this regime. These impacts diminish with decreasing w_{age}.

Stratification increases hub height wind speeds and increases the vertical shear of the mean wind across the rotor plane. Fortuitously, this stability-induced enhanced shear does not influence turbulence intensity at hub height, but does increase (decrease) turbulence intensity below (above) hub height. Increased stability also increases the wave-induced pressure stress by $\sim$10%.

In a broad sense, these results suggest that one needs information on winds, temperature, and *wave state* to upscale buoy measurements to hub-height and across the rotor plane. Wind-wave alignment likely explains large scatter in non-dimensional surface roughness $z_\circ/H_s$ under swell-dominated conditions (*i.e.* at low inverse wave age w_{age}^{-1}). Andreas et al.'s (2012) relationship between u_* and the 10-m wind speed under predicts the increased u_* produced by wave-induced pressure drag. Incorporating wave-state (speed and direction) influences in parameterizations improves predictive skill.

6.2 Importance of Fetch in the Coastal Zone

At CBLAST-Low, relatively strong jet speeds of 10–15 $\mathrm{m\,s^{-1}}$ occur at the top of the weakly stable boundary layer at about 100 m. When winds are offshore, advection of warm air from land increases the atmospheric stability.

The low-level jet varies significantly between subsequent soundings on time scales of tens of minutes or less. This variability is generally coherent only over small depths. The negative speed shear above the wind maximum is large, and the turbulence at these levels can be significant for individual soundings. The relative variation of the wind and turbulence among the soundings is much greater than that for temperature. Nonetheless, the jet remains persistent within each observational period of several hours.

Off the East Coast of the United States during CBLAST-Low, cases with short fetch include thin stable boundary layers with depths of only a few tens of meters. In the coastal zone, the relationship between the mean wind and the surface fiction velocity ($u_*(V)$) is significantly related to wind direction for weak winds but is not systematically related to the air sea difference of virtual potential temperature, $\delta\theta_v$; since waves generally propagate from the south at the ASIT tower, these results suggest that under weak wind conditions waves likely influence surface stress more than stratification does.

Winds and waves are frequently misaligned in the coastal zone. Stability conditions persist for long duration. Over a four year period, FINO1 (with long fetch) primarily experienced weakly-unstable conditions, while stability at ASIT (with a larger influence of offshore winds) experiences a mix of both unstable and stable conditions, where the summer months are predominantly stable.

The relationship of $u_*(V)$ with $\delta\theta_v$ is very weak except for stronger offshore flow with short fetch. Semi-decoupling with the sea surface is not observed at the ASIT site because large warm air advection requires sufficiently strong winds that apparently limits $\delta\theta_v$ through vertical mixing. Although the relationship between $u_*(V)$ and $\delta\theta_v$ is weak (or undetectable), the variation of z/L accounts for relatively large variation of $\phi_m(z/L)$ for this data set (Edson et al., 2013). However, z/L is not a true external stability parameter but rather a quantification of the turbulence itself. This may explain why $\delta\theta_v$ can be relatively unimportant yet the turbulence and nondimensional shear are sensitive to the value of z/L.

6.3 Market Barriers

In combination, our project has yielded important information regarding the impact two physical processes (non-equilibrium wind/waves and stratification) have on the atmosphere within which offshore turbines operate. This knowledge should help guide and inform those making critical decisions surrounding design criteria of future turbines to be deployed in the coastal zone.

Reductions in annually averaged hub height wind speed error reduction using our new surface layer parameterization that accounts for wave state are relatively modest. However wind turbine power production depends on the wind speed cubed, therefore the error in estimated power production translates to $\sim$5% (where, this power production error reduction estimate was computed as the ratio between the difference between annually averaged hub height wind speed from the two simulations and the observed hub height wind speed). This reduction in estimated power production is therefore significant and can substantially impact wind resource assessment and decision making regarding the a particular wind plant location's viability. For specific cases, significant reductions in wind speed prediction errors (*e.g.,* Fig. 22) can yield substantially improved wind power forecast skill, thereby mitigating costs and/or increasing revenue through improved: 1) long-term forecasting for planning maintenance operations, 2) day-ahead forecasting for power trading and resource allocation, and 3) short-term forecasting for dispatch and grid balancing.

7. Recommendations

Although surface waves and coastal boundary layers are individually mature subjects, the present work illustrates the importance of understanding their mutual coupling for offshore wind energy applications. Further improvements in predicting offshore coastal winds need to embrace this coupling by focusing on observations, turbulence simulations, and boundary-layer parameterizations in forecast models. In particular we suggest that the offshore wind community would benefit from:

Targeted observations:

- Surface layer
  - At or below 10m ASL
  - Wind speed, direction
  - Temperature
  - Turbulent fluxes of momentum and heat
- Directional wave spectrum (add to buoy network?)
- SST
- Mean vertical profiles up to and through the rotor plane (by light detection and ranging (LiDAR)? or unmanned aerial vehicle (UAV)?)
  - Wind
  - Temperature
- Large-scale 3D pressure and wind measurements to evaluate baroclinicity
- ABL depth
- Free access for the broad community
- Mandate that developers collect observations adhering to a defined standard and that that data be made publicly availability within the permitting process?
- Long term observations (years) but at sufficiently high frequency to capture the turbulence (faster than 1 Hz), where the faster than 1 Hz data needs to be available to the community as well as mean statistics.

Turbulence resolving simulation:

- Swell propagating in different directions from locally growing waves
- Observed 2D, time-evolving waves (Wave and Surface Current Monitoring System (WAMOS-II))
- With waves that respond to wind forcing

Weather forecasting – wave model integration:

- Integrated wave model in WRF (*e.g.,*Wavewatch III?)
- Ability to assimilate wave data

- Coupled atmosphere-ocean modeling to bring ocean influences into weather forecasts

Theory advancement:

- Determine underpinnings of wind/water coupling and capillary wave growth

References

Andreas, E. L., L. Mahrt, and D. Vickers, 2012: A new drag relation for aerodynamically rough flow over the ocean. *J. Atmos. Sci.*, **69 (8)**, 2520–2537, doi:10.1175/JAS-D-11-0312.1.

Barthelmie, R. J., 1999: The effects of atmospheric stability on coastal wind climates. *Meteorol. Appl.*, **6 (1)**, 39–47, doi:10.1017/s1350482799000961.

Beardsley, R. C., C. E. Dorman, C. A. Friehe, L. K. Rosenfeld, and C. D. Winant, 1987: Local atmospheric forcing during the Coastal Ocean Dynamics Experiment: 1. A description of the marine boundary layer and atmospheric conditions over a northern California upwelling region. *J. Geophys. Res.*, **92 (C2)**, 1467, doi:10.1029/JC092iC02p01467.

Beare, R. J., and Coauthors, 2006: An intercomparison of large-eddy simulations of the stable boundary layer. *Boundary-Layer Meteorol.*, **118 (2)**, 247–272, doi:10.1007/s10546-004-2820-6.

Charnock, H., 1955: Wind stress on a water surface. *Quart. J. Roy. Meteorol. Soc.*, **81**, 639–640, doi:10.1002/qj.49708135027.

Crawford, T. L., and R. J. Dobosy, 1992: A sensitive fast-response probe to measure turbulence and heat flux from any airplane. *Boundary-Layer Meteorol.*, **59 (3)**, 257–278, doi: 10.1007/BF00119816.

Csanady, G. T., 2001: *Air-sea interaction: Laws and mechanisms*. Cambridge University Press, Cambridge, United Kingdom, 239 pp., doi:10.1017/CBO9781139164672.

Davis, K. J., N. Gamage, C. R. Hagelberg, C. Kiemle, D. H. Lenschow, and P. P. Sullivan, 2000: An objective method for deriving atmospheric structure from airborne lidar observations. *J. Atmos. Ocean. Tech.*, **17**, 1455–1468, doi:10.1175/1520-0426(2000)017⟨1455:AOMFDA⟩2.0.CO;2.

Donelan, M. A., J. Hamilton, and W. H. Hui, 1985: Directional spectra of wind-generated waves. *Phil. Trans. Roy. Soc. London, Ser. A*, **315 (1534)**, 509–562, doi:10.1098/rsta.1985.0054.

Drennan, W. M., H. C. Graber, D. Hauser, and C. Quentin, 2003: On the wave age dependence of wind stress over pure wind seas. *J. Geophys. Res.*, **108 (C3)**, 8062, doi:10.1029/2000JC000715.

Drennan, W. M., P. K. Taylor, and M. J. Yelland, 2005: Parameterizing the sea surface roughness. *J. Phys. Ocean.*, **35**, 835–848, doi:10.1175/JPO2704.1.

Edson, J., and Coauthors, 2007: The coupled boundary layers and airsea transfer experiment in low winds. *Bull. Amer. Meteorol. Soc.*, **88 (3)**, 341–356, doi:10.1175/BAMS-88-3-341.

Edson, J. B., and Coauthors, 2013: On the exchange of momentum over the open ocean. *J. Phys. Ocean.*, **43 (8)**, 1589–1610, doi:10.1175/JPO-D-12-0173.1.

Geernaert, G. L., F. Hansen, M. Courtney, and T. Herbers, 1993: Directional attributes of the ocean surface wind stress vector. *J. Geophys. Res.*, **98 (C9)**, 16 571, doi:10.1029/93JC01439.

Hanley, K. E., and S. E. Belcher, 2008: Wave-driven wind jets in the marine atmospheric boundary layer. *J. Atmos. Sci.*, **65 (8)**, 2646–2660, doi:10.1175/2007JAS2562.1.

Hanley, K. E., S. E. Belcher, and P. P. Sullivan, 2010: A global climatology of windwave interaction. *J. Phys. Ocean.*, **40 (6)**, 1263–1282, doi:10.1175/2010JPO4377.1.

Jiménez, P. A., and J. Dudhia, 2015: On the wind stress formulation over shallow waters in atmospheric models. *Geosci. Model Dev. Discuss.*, 9063–9077, doi:10.5194/gmdd-7-9063-2014.

King, J. C., T. A. Lachlan-Cope, R. S. Ladkin, and A. Weiss, 2008: Airborne measurements in the stable boundary layer over the Larsen Ice Shelf, Antarctica. *Boundary-Layer Meteorol.*, **127 (3)**, 413–428, doi:10.1007/s10546-008-9271-4.

Komen, G. J., L. Cavaleri, M. Donelan, K. Hasselmann, S. Hasselmann, and P. A. E. M. Janssen, 1994: *Dynamics and Modelling of Ocean Waves*. Cambridge University Press, Cambridge, United Kingdom, 532 pp.

Lange, B., H. K. Johnson, S. Larsen, J. Højstrup, H. Kofoed-Hansen, and M. J. Yelland, 2004: On detection of a wave age dependency for the sea surface roughness. *J. Phys. Ocean.*, **34**, 1441–1458, doi:10.1175/1520-0485(2004)034⟨1441:ODOAWA⟩2.0.CO;2.

Mahrt, L., 2010: Computing turbulent fluxes near the surface: Needed improvements. *Agric. For. Meteorol.*, **150 (4)**, 501–509, doi:10.1016/j.agrformet.2010.01.015.

Mahrt, L., D. Vickers, and E. L. Andreas, 2014: Low-level wind maxima and structure of the stably stratified boundary layer in the coastal zone. *J. Appl. Meteorol. Clim.*, **53**, 363–376, doi:10.1175/JAMC-D-13-0170.1.

Musial, W., and B. Ram, 2010: Large-scale offshore wind power in the United States: Assessment of opportunities and barriers. National Renewable Energy Laboratory Technical Report NREL/TP-500-4075, Golden, CO, 221 pp.

Nakanishi, M., and H. Niino, 2004: An improved Mellor-Yamada level-3 model with condensation physics: Its design and verification. *Boundary-Layer Meteorol.*, **112**, 1–31.

Nakanishi, M., and H. Niino, 2006: An improved Mellor-Yamada level 3 model: Its numerical stability and application to a regional prediction of advecting fog. *Boundary-Layer Meteorol.*, **119**, 397–407.

Phillips, O. M., 1977: *The dynamics of the upper ocean*. Cambridge University Press, 336 pp.

Saha, S., 2010: The NCEP climate forecast system reanalysis. *Bull. Amer. Meteorol. Soc.*, **91**, 1015–1057, doi:10.1175/2010Bams3001.2.

Skamarock, W. C., and Coauthors, 2008: A Description of the Advanced Research WRF Version 3. National Center for Atmospheric Research Techical Note, NCAR/TN-468+STR, Boulder, CO, 88 pp.

Skyllingstad, E. D., D. Vickers, L. Mahrt, and R. Samelson, 2007: Effects of mesoscale sea-surface temperature fronts on the marine atmospheric boundary layer. *Boundary-Layer Meteorol.*, **123**, 219–237, doi:10.1007/s10546-006-9127-8.

Smedman, A., U. Högström, H. Bergström, and A. Rutgersson, 1999: A case study of air-sea interaction during swell conditions. *J. Geophys. Res.*, **104**, 25 833–25 851.

Smedman, A., U. Högström, E. Sahleé, W. M. Drennan, K. K. Kahma, H. Pettersson, and F. Zhang, 2009: Observational study of marine atmospheric boundary layer characteristics during swell. *J. Atmos. Sci.*, **66**, 2747–2763, doi:10.1175/2009JAS2952.1.

Stull, R. B., 1988: *An introduction to boundary layer meteorology*. Kluwer Academic Publishers, Dordrecht, The Netherlands, 666 pp., doi:10.1007/978-94-009-3027-8.

Sullivan, P. P., J. B. Edson, T. Hristov, and J. C. McWilliams, 2008: Large-eddy simulations and observations of atmospheric marine boundary layers above nonequilibrium surface waves. *J. Atmos. Sci.*, **65 (4)**, 1225–1245, doi:10.1175/2007JAS2427.1.

Sullivan, P. P., J. C. McWilliams, and E. G. Patton, 2014: Large-eddy simulation of marine atmospheric boundary layers above a spectrum of moving waves. *J. Atmos. Sci.*, **71 (11)**, 4001–4027, doi:10.1175/JAS-D-14-0095.1.

Sullivan, P. P., C.-H. Moeng, B. Stevens, D. H. Lenschow, and S. D. Mayor, 1998: Structure of the entrainment zone capping the convective atmospheric boundary layer. *J. Atmos. Sci.*, **55**, 3042–3064, doi:10.1175/1520-0469(1998)055⟨3042:SOTEZC⟩2.0.CO;2.

Sullivan, P. P., and E. G. Patton, 2011: The effect of mesh resolution on convective boundary layer statistics and structures generated by large-eddy simulation. *J. Atmos. Sci.*, **68 (10)**, 2395–2415, doi:10.1175/JAS-D-10-05010.1.

Sullivan, P. P., E. G. Patton, and K. W. Ayotte, 2010: Turbulent flow over and around sinusoidal bumps, hills, gaps and craters derived from large eddy simulations. *19th Conf. Bound. Layer Turbul.*, American Meteorological Society, Keystone, CO, Paper 1B.5.

Sun, J., D. Vandemark, L. Mahrt, D. Vickers, T. Crawford, and C. Vogel, 2001: Momentum transfer over the coastal zone. *J. Geophys. Res.*, **106 (D12)**, 12 437–12 448, doi:10.1029/2000JD900696.

Tambke, J., M. Lange, U. Focken, J.-O. Wolff, and J. A. T. Bye, 2005: Forecasting offshore wind speeds above the North Sea. *Wind Energy*, **8 (1)**, 3–16, doi:10.1002/we.140.

Taylor, P. K., and M. J. Yelland, 2001: The dependence of sea surface roughness on the height and steepness of the waves. *J. Phys. Ocean.*, **31**, 572–590, doi:10.1175/1520-0485(2001)031⟨0572:TDOSSR⟩2.0.CO;2.

Toba, Y., S. D. Smith, and N. Ebuchi, 2001: Historical drag expressions. *Wind Stress over the Ocean*, I. S. F. Jones, and Y. Toba, Eds., Cambridge University Press, Cambridge, U. K., chap. 2, 35–53.

Wharton, S., and J. K. Lundquist, 2012a: Assessing atmospheric stability and its impacts on rotor-disk wind characteristics at an onshore wind farm. *Wind Energy*, **15**, 525–546, doi:10.1002/we.483.

Wharton, S., and J. K. Lundquist, 2012b: Atmospheric stability affects wind turbine power collection. *Environ. Res. Lett.*, **7 (1)**, 9, doi:10.1088/1748-9326/7/1/014005.

Winant, C. D., C. E. Dorman, C. A. Friehe, and R. C. Beardsley, 1988: The marine layer off Northern California: An example of supercritical channel flow. *J. Atmos. Sci.*, **45 (23)**, 3588–3605, doi:10.1175/1520-0469(1988)045⟨3588:TMLONC⟩2.0.CO;2.